The Astrophysical Journal, 929:129 (28pp), 2022 April 20 https://doi.org/10.3847/1538-4357/ac5a49

EXORCISM: A Spectroscopic Survey of Young Eruptive Variables (EXor and Candidates)

T. Giannini[1], A. Giunta[2], M. Gangi[1], R. Carini[1], D. Lorenzetti[1], S. Antoniucci[1], A. Caratti o Garatti[3,4], L. Cassará[5], B. Nisini[1], A. Rossi[6], V. Testa[1], and F. Vitali[1]
[1] INAF—Osservatorio Astronomico di Roma, via Frascati 33, I-00078, Monte Porzio Catone, Italy
[2] ASI—Agenzia Spaziale Italiana—Via del Politecnico, I-00133 Roma, Italy
[3] INAF—Osservatorio Astronomico di Capodimonte, Via Moiariello 16, I-80131 Napoli, Italy
[4] Dublin Institute for Advanced Studies, School of Cosmic Physics, Astronomy & Astrophysics Section, 31 Fitzwilliam Place, Dublin 2, Ireland
[5] INAF-IASF Milano, via Alfonso Corti 12, I-20129 Milano, Italy
[6] INAF-Osservatorio di Astrofisica e Scienza dello Spazio, Via Piero Gobetti, 93/3, I-40129 Bologna, Italy
Received 2021 June 7; revised 2022 January 19; accepted 2022 March 1; published 2022 April 20

Abstract

We present an optical/near-IR survey of 11 variable young stars (EXors and EXor candidates) aimed at deriving and monitoring their accretion properties. About 30 optical and near-infrared spectra ($\Re \sim 1500$–2000) were collected between 2014 and 2019 with the Large Binocular Telescope (LBT). From the spectral analysis we have derived the accretion luminosity ($L_{\rm acc}$) and mass accretion rate ($\dot{M}_{\rm acc}$), the visual extinction ($A_{\rm V}$), the temperature and density of the permitted line formation region (T, $n_{\rm H}$), and the signature of the outflowing matter. Two sources (ASASSN-13db and iPTF15afq) have been observed in outburst and quiescence, three during a high level of brightness (XZ Tau, PV Cep, and NY Ori), and the others in quiescence. These latter have $L_{\rm acc}$ and $\dot{M}_{\rm acc}$ in line with the values measured in classical T Tauri stars of similar mass. All sources observed more than once present $L_{\rm acc}$ and $\dot{M}_{\rm acc}$ variability. The most extreme case is ASASSN-13db, for which $\dot{M}_{\rm acc}$ decreases by two orders of magnitude from the outburst peak in 2015 to quiescence in 2017. Also, in NY Ori $L_{\rm acc}$ decreases by a factor 25 in one year. In 80% of the sample we detect the [O I] 6300 Å line, a tracer of mass loss. From the variability of the Hα/[O I] 6300 Å ratio, we conclude that mass accretion variations are larger than mass loss variations. From the analysis of the H I recombination lines, a correlation is suggested between the density of the line formation region, and the level of accretion activity of the source.

Unified Astronomy Thesaurus concepts: Star formation (1569); Pre-main sequence stars (1290); Eruptive phenomena (475); Stellar mass loss (1613)

1. Introduction

EXor objects (named after the prototype EX Lupi, Herbig 1989) are Pre-Main Sequence (PMS) stars showing episodes of eruptive accretion caused by magnetospheric accretion events (Shu et al. 1994). Since the unsteady mass accretion is a central theme in the star formation process (e.g., Cieza et al. 2018), these objects have been the subject of many investigations (Kuffmeier et al. 2018; Contreras Peña et al. 2019; Meng et al. 2019; MacFarlane et al. 2019a, 2019b; see also Audard et al. (2014) for a comprehensive view of the EXor phenomenon). EXors are characterized by outbursts of short duration (typically months) occurring at different timescales (months, years) and showing amplitudes of several magnitudes at optical and near-IR wavelengths. An evolutionary scheme has been proposed in which EXors represent a less energetic and (possibly) later stage than the powerful FU Orionis eruptions (FUors, Hartmann & Kenyon 1985; Hartmann et al. 1993), although EXors present substantial differences, such as shorter and more frequent outbursts, spectra dominated by emission lines instead of absorption lines, and smaller values of the mass accretion rate during outbursts (10^{-7}–10^{-6} $M_\odot$ yr^{-1} versus 10^{-5}–10^{-4} $M_\odot$ yr^{-1}). Yet, at present, a detailed model for the disk structure and its evolution does not exist for EXors and different hypotheses have been proposed for the possible trigger of their outbursts: thermal instability in the disk (e.g., Audard et al. 2014 and references therein), gravitational perturbations induced by a binary companion (Lodato & Clarke 2004) or by the migration of a giant planet (Bonnell & Bastien 1992), or sudden changes in the stellar magnetic activity (D'Angelo & Spruit 2012; Armitage 2016).

Observational constraints to theoretical models are nowadays provided by photometric monitoring programs (e.g., Grankin et al. 2008; Morales-Calderón et al. 2011; Guo et al. 2020) and by ongoing all-sky surveys (e.g., Gaia,[7] All-Sky Automated Survey for Supernovae (ASASSN),[8] Intermediate Palomar Transient Factory (iPTF),[9] Panoramic Survey Telescope & Rapid Response System (Pan-STARSS)[10], and VISTA Variables in the Via Lactea (VVV),[11]) which systematically follow (although often at a poor level of sensitivity) the photometric variations of many EXors and EXor candidates, thus allowing us to track the changes of their integrated properties (light curves, spectral energy distributions (SEDs), and colors). A dramatic improvement in this context will be provided in the next future by the the Vera Rubin Observatory,[12] which will

[7] https://sci.esa.int/web/gaia
[8] http://www.astronomy.ohio-state.edu/asassn/index.shtml
[9] https://www.ptf.caltech.edu/iptf
[10] https://panstarrs.stsci.edu/
[11] https://vvvsurvey.org/
[12] https://www.lsst.org/

Table 1
The Investigated Sample

Simbad Name	R.A. (J2000) (h:m:s)	Decl. (J2000) (°:′:″)	D^1 (pc)	Location	Binarity	Jet/Outflow	Other Designation	Ref
EXors								
XZ Tau	04:31:40.07	+18:13:57.2	150[a]	L1551	Y(0.″30)	HH152/Y	Haro6-15−SVS169	1
UZ Tau E	04:32:43.07	+25:52:31.0	130.4	B19	Y(0.″34)	⋯/⋯	UZ Tau A	2
VY Tau	04:39:17.41	+22:47:53.4	153.4	L1536	Y(0.″66)	Y(?)/⋯	SVS38	3,4
NY Ori	05:35:36.01	−05:12:25.3	403.5	ONC	⋯	⋯/⋯	Parenago 2119	5
V1143 Ori	05:38:03.90	−04:16:42.8	395.3	L1640	⋯	⋯/⋯	Sugano's obj	5
EXor candidates								
DR Tau	04:47:06.21	+16:58:42.8	193.0	L1558	N	Y/⋯	⋯	6
ASASSN-13db	05:10:11.08	−03:28:26.3	387.1	near L1615/16	⋯	⋯	⋯	⋯
V1647 Ori	05:46:13.14	−00:06:04.9	412.9	Mc Neil's nebula	N(?)	HH23(?)/Y	Mc Neil's Nebula	7,8,9
iPTF15afq	07:09:21.40	−10:29:34.4	1315.7	CMa	⋯	⋯/⋯	2MJ07092139-1029344	10,11,12
PV Cep	20:45:53.94	+67:57:38.7	356.5	L1158	N	HH315/Y	⋯	13
V350 Cep	21:43:00.01	+66:11:28.0	872.5	NG7129	⋯	⋯/⋯	⋯	5

Note. 1: Distances taken from GAIA EDR3 (Gaia Collaboration et al. (2016), Gaia Collaboration et al. (2021); [a] assumed. References: 1, Coffey et al. (2004); 2, Jensen et al. (2007); 3, Leinert et al. (1993); 4, Banzatti et al. (2019); 5, Herbig (2008); 6, Kun et al. 2016; 7, Arce et al. (2010); 8, Young et al. (2015); 9, Akeson et al. (2019); 10, Joncour et al. (2017); 11, Li et al. (2015); 12, Banzatti et al. (2014); 13, Principe et al. (2018).

explore the southern sky with unprecedented sensitivity and cadence.

Conversely, the optical and IR spectroscopic monitoring of the EXors is currently not at a comparable level of sky coverage and cadence, despite its crucial importance for understanding how the gas properties (e.g., excitation, ionization, dynamics) vary during different activity phases. Indeed, so far, only few EXors have been spectroscopically investigated (e.g., EX Lupi: Sipos et al. 2009; Sicilia-Aguilar et al. 2012V2492 Cyg: Hillenbrand et al. 2013; V1118 Ori: Audard et al. 2010; Lorenzetti et al. 2015; Giannini et al. 2016, 2017, 2020; HBC722: Kóspál et al. 2016). In addition, Guo et al. (2020) recently presented a near-IR spectroscopic monitoring of a few VISTA variables (supposedly eruptive candidates).

Waiting for instruments like SoXS[13] at ESO-NTT (Schipani et al. 2018), which will be specifically dedicated to the spectroscopic monitoring of large samples of objects, we have started in 2014 the EXOR OptiCal and Infrared Systematic Monitoring program EXORCISM (Antoniucci et al. 2013). Over the years, new EXor candidates have been discovered and included in our database. As a result, we provide here the first flux-limited deep spectroscopic atlas of EXors (and candidates) collected through state-of-the-art instrumentation (Large Binocular Telescope, LBT) at optical and near-IR wavelengths. As outburst phases are expected to be short-lived and rare events, most of our spectra have been taken during quiescence phases. These spectra allow us to infer the baseline values of the physical parameters, such as intrinsic line fluxes, accretion luminosity ($L_{\rm acc}$), and mass accretion rate ($\dot{M}_{\rm acc}$), which can be used as reference in case of outburst. This is what we did for the few sources that we observed both in quiescence and outburst, for which we were able to study the variation of the parameters between the two phases.

The paper is organized as follows: Section 2 gives general information on the investigated sample while Section 3 provides details on the observations and data reduction procedures. In Section 4, we comment on the light curves of the individual sources. Sections 5 and 6 are dedicated to the description of the spectra and to the discussion of the results obtained from the spectroscopic analysis. Final remarks are given in Section 7.

2. The Investigated Sample

Table 1 lists our targets with their general properties. It provides coordinates, distance, location, binarity, and jet or outflow detection. Together with the name given in the Simbad Astronomical Database[14], we report other designation(s) commonly used in the literature.

Our sample is divided into two groups. The first is composed of five known EXors (XZ Tau, UZ Tau E, VY Tau, NY Ori, V1143 Ori) listed in the compilation by Audard et al. (2014) and confirmed by many works in literature as members of the class. In addition, we have also obtained multi-epoch spectroscopy of the classical EXor V1118 Ori at both optical and IR wavelengths. These data are not discussed here since they have been separately presented in a series of dedicated papers (Giannini et al. 2020 and references therein).

The second group, generically named as "EXor candidates" in Table 1, consists of six sources that have been reported through different alerts (e.g., astronomers' telegrams and public surveys alerts) for being young and highly variables objects ($\Delta V \gtrsim 2$ mag). Here we briefly comment on each of them. Two objects, namely V1647 Ori and PV Cep, are present in the Audard et al. (2014) compilation, but their nature is still controversial. V1647 Ori has been previously classified as a candidate FUor, but it is currently considered as a peculiar object, since its spectrum now differs significantly from that of a bona fide FUor (Connelley & Reipurth 2018), showing both FUor and EXor features. A few more objects with similar characteristics have been identified during the VVV spectroscopic survey and dubbed "MNors" (Contreras Peña et al. 2017). PV Cep and DR Tau were originally included in the first list of EXor variables by Herbig (1989). PV

[13] https://www.eso.org/sci/facilities/develop/instruments/SoXS.html

[14] http://simbad.u-strasbg.fr/simbad/

Table 2
Photometric Variability

ID	$mag_{min}-mag_{max}$ (mag)	Band[a]	Bursts	Ref
EXors				
XZ Tau	16.6−10.4	V	many/last 2014−2016	1,2
UZ Tau E	18.5−12.5	V	many/last 2006	3,4
VY Tau	15.3−9.0	V	1960–1972/ last 2014	2,3,5,6
NY Ori	>16−13.3	V	many/last 2001	7,8
V1143 Ori	16.7−13.5	V	many/last 1993	7,8
EXor candidates				
DR Tau	16.0−10.5	V	1960−1980	3,9,10,11
ASASSN-13db	>17−13.2	V	2013,2014-2017	12,13
V1647 Ori	23.0−17.8	r′	1966,2003, 2008	14,15,16,17
iPTF15afq	19.0−16.7	R	2015,2019	18,19
PV Cep	16−11	R	1977,1979,2008	20,21,22
V350 Cep	>21−16.5	B	1978–2005	7,22,23

Note. References: 1, Coffey et al. (2004); 2, Dodin et al. (2016); 3, Herbig & Bell (1988); 4, Jensen et al. (2007); 5, Herbig (1990); 6, Stone (1983); 7, Herbig (2008); 8, Jurdana-Šepić et al. (2017); 9, Chavarria (1979); 10, Kenyon et al. (1994); 11, Grankin et al. (2007); 12, Holoien et al. (2014); 13, Sicilia-Aguilar et al. (2017); 14, Briceño et al. (2004); 15, Aspin et al. (2006); 16, Aspin et al. (2008); 17, Aspin & Reipurth (2009); 18, Miller et al. (2015); 19, Hillenbrand (2019); 20, Cohen et al. (1981); 21, Caratti o Garatti et al (2013); 22, Lorenzetti et al. (2011); 23, Jurdana-Šepić et al. (2018).

Cep repeatedly undergoes intense outbursts (up to 5 mag) of short duration and brightness between that of FUors and EXors (Andreasyan et al. 2021). Its high luminosity ($\approx 100\,L_{\odot}$) is likely attributable to a young Herbig Ae star (see e.g., Lorenzetti et al. 2011). DR Tau has progressively increased its brightness by about three magnitudes between 1960 and 1980. Since then, its average brightness has been at the same level but still with remarkable photometric fluctuations with amplitude up to ∼1 mag in the optical (Banzatti et al. 2014 and references therein). Similarly, the *B* magnitude of V350 Cep changed from >21 to ∼17 between 1954 and 1978. Afterward, the source has remained at roughly the same level of brightness, with the exception of at least two fading events of about 2 mag in *B* in 1979 and 2004. For these reasons Herbig (2008) did not classify V350 Cep as an EXor. Considering its high and stable brightness level and its spectrum rich in emission lines, it is likely that also V350 Cep is an object with properties in between those of FUors and EXors (Andreasyan et al. 2021). iPTF15afq is a new candidate EXor, suggested by Miller et al. (2015) on the basis of the amplitude of its outburst of about 2.5 mag (in *R*-band) and its spectrum dominated by lines in emission. ASASSN-13db (discovered by the ASASSN survey) has been originally classified as an EXor by Holoien et al. (2014). Later observations of blueshifted absorption features in several hydrogen and metallic lines suggest an intermediate behavior between EXors and FUors (Sicilia-Aguilar et al. 2017).

In Table 2, we summarize the photometric properties of the sources, with the range of variation observed in the indicated band and a short (non-exhaustive) summary of the variability history as retrieved from the literature.

In Table 3, we list the relevant stellar parameters as given in the literature, namely the visual extinction (A_V), bolometric (L_{bol}), stellar (L_*) and accretion (L_{acc}) luminosity, spectral type (SpT) and effective temperature (T_{eff}), stellar mass (M_*), mass accretion rate ($\dot{M}_{acc}$), and evolutionary class (typically derived from the spectral slope between 2 and 24 μm). All sources but PV Cep, have mass $\lesssim 1\,M_{\odot}$ and spectral types M-K. V1647 Ori and PV Cep present a high and variable A_V while all other sources are only slightly extincted. Mass accretion rates have been measured for about 70% of the sample. During quiescence, they are typically of the order of 10^{-8}–$10^{-7}\,M_{\odot}\,yr^{-1}$, but show variations up to several orders of magnitude in bursts.

In summary, our sample is composed of sources whose variability may differ in amplitude, cadence, and duration. In all cases, however, the increase of brightness has been attributed in the literature to accretion events, sometimes accompanied by significant variations of the local extinction.

3. Observations and Data Reduction

The observations were carried out between 2014 and 2019 with the 8.4 m Large Binocular Telescope (LBT) located at Mount Graham (Arizona, USA). Optical and near-IR spectra of the targets were obtained with the Multi-Object Double Spectrograph (MODS, Pogge et al. 2010) and the LBT Utility Camera in the Infrared (LUCI, Seifert et al. 2003), respectively.

Given the remarkable brightness of the sources, our project was executed as a filler program during unfavorable atmospheric conditions that usually make observations of weaker sources unfeasible. As a consequence, we were not able to complete the survey with all the needed spectra. However, the poor photometric quality of the sky (typical seeing $\gtrsim 1\farcs5$) did not represent a significant problem for the validity of our results, since the flux calibration of the spectra was based on photometric observations taken close in time to the spectra.

In total, we acquired 19 spectra with MODS (11 targets) and 10 spectra with LUCI (8 targets), see the journal of observations in Table 4. Optical and near-IR spectra have been taken during the same night only for V1647 Ori, and for DR Tau at a temporal distance of 4 days. For all the other targets, optical and near-IR spectra are spaced by several months or years, and, in some cases, the spectrum of one of the two segments is missing.

MODS observations were performed with the dual grating mode (blue + red channels, spectral range 350−950 nm) by using a $0\farcs80$ slit ($\Re \sim 1500$ and 1800 in the blue and red channels, respectively). The slit angle matched the parallactic angle to minimize the wavelength dependence on the slit transmission. For each source, the adopted integration time is reported in Table 4.

LUCI observations were carried out with the G200 low-resolution grating coupled with the $0\farcs75$ slit. Two data sets were acquired with the standard ABB'A' technique using the *zJ* and *HK* grisms. This provides a final spectrum covering the 1.0−2.4 μm wavelength range at $\Re \sim 1500$. The integration time for the individual sources is provided in Table 4.

Data reduction was performed at the Italian LBT Spectroscopic Reduction Center[15], by means of scripts optimized for LBT data. Data reduction steps of each MODS spectral-image are correction for dark and bias, bad-pixel mapping,

[15] http://www.iasf-milano.inaf.it/Research/lbt_rg.html

Table 3
Stellar Parameters

Name	A_V (mag)	L_{bol} ($L_\odot$)	SpT	L_* ($L_\odot$)	T_{eff} (K)	M_* ($M_\odot$)	L_{acc} ($L_\odot$)	$\dot{M}_{acc}$ ($10^{-7} M_\odot$ yr^{-1})	Class	Ref
EXors										
XZ Tau	1.4−1.5	4.2−10.7	M3	0.57	3410	0.37	0.347	1−10, 0.14	II	1,2,3,4
UZ Tau E	0.5−1.5	1.7	M3	0.62	3410	0.3	0.025	1−3	II	1,4,5,6
VY Tau	0.5−0.85	0.72	M1.5	0.39	3640	0.39	⋯	⋯	II	1,7,8
NY Ori	0.3	⋯	K4	⋯	4430	1.0	⋯	⋯	⋯	9,10
V1143 Ori	0	⋯	M2	0.20	3500	0.5	⋯	⋯	II	7
EXor candidates										
DR Tau	0.45−1.6	1.2	K7	0.32	4070	0.75	0.74	4−9	II	1,4,11,12,13
ASASSN-13db	0.04	0.1	M5	0.03	3070-4855	0.15	$<4\ 10^{-4}$ − 0.2	0.01−3.3	II	14,15
V1647 Ori	10−20	9.5−90	M0	5.20	3800	0.8	3.5−16	0.2−38	I/f	16,17,18,19,20
iPTF15afq	⋯	⋯	⋯	⋯	⋯	⋯	⋯	⋯	I	21
PV Cep	10.8−12	41−100	G4	17.0	5500	2.4−4	5.7−80	2−50	⋯	22,23,24,25,26,27
V350 Cep	⋯	⋯	M0	⋯	3560–3900	⋯	⋯	⋯	⋯	28

Note. References: 1, Herczeg & Hillenbrand (2014); 2, Osorio et al. (2016); 3, Hartigan & Kenyon (2003); 4, Csépány et al. (2017); 5, Yang et al. (2012); 6, Lorenzetti et al. (2007); 7, Sipos & Kóspál (2014); 8, Cabrit et al. (1990); 9, Hillenbrand (1997); 10, Kounkel et al. (2019); 11, Muzerolle et al. (2003); 12, Lorenzetti et al. (2009); 3, Petrov et al. (2011); 14, Holoien et al. (2014); 15, Sicilia-Aguilar et al. (2017); 16, Aspin (2011); 17, Andrews et al. (2004); 18, Gramajo et al. (2014); 19, Moody & Stahler (2017); 20, Aspin et al. (2008); 21, Fischer et al. (2016); 22, Kun et al. (2011); 23, Hamidouche (2010); 24, Magakian & Movsesian (2001); 25, Cohen et al. (1981); 26, The et al. (1994); 27, Caratti o Garatti et al. (2013); 28, Kun et al. (2009).

Table 4
Journal of Observations

Source	MODS					LUCI				
	Date (yy/mm/dd)	MJD	T_{int} (B/R) (s)	Phot[a] (mag)	Filter	Date (yy/mm/dd)	MJD	T_{int} (zJ/HK) (s)	Phot[a] (mag)	Filter
XZ Tau	2014/12/21	57012	600/600	12.54	r	⋯	⋯	⋯	⋯	⋯
	2018/03/21	58198	1200/1200	13.68	r	⋯	⋯	⋯	⋯	⋯
UZ Tau E	2014/12/22	57013	600/600	12.21	r	2016/01/25	57412	120/88	7.94	[Fe II]1.64
VY Tau	2014/12/21	57012	600/600	12.88	r	2016/03/04	57451	160/80	9.43	[Fe II]1.64
NY Ori	2014/12/21	57012	600/600	11.94	r	⋯	⋯	⋯	⋯	⋯
	2016/01/31	57418	600/600	14.05	r	⋯	⋯	⋯	⋯	⋯
V1143 Ori	2014/12/21	57012	1200/1200	16.23	r	⋯	⋯	⋯	⋯	⋯
DR Tau	2014/10/31	56961	150/150	12.31[1] (−1)	V	2018/03/23	58200	30/30	9.08	*J*
	2018/03/19	58196	1200/1200	11.92	r	⋯	⋯	⋯	⋯	⋯
ASASSN-13db	2014/12/21	57012	1200/1200	13.94	g	2015/02/10	57063	1200/1200	10.65	*H*
	2015/10/01	57296	1200/1200	13.95	g	⋯	⋯	⋯	⋯	⋯
	2017/02/21	57805	1200/1200	17.66	r	⋯	⋯	⋯	⋯	⋯
V1647 Ori	2016/01/26	57413	⋯ /1200	18.68	r	2016/01/26	57413	1200/600	12.10	*J*
iPTF15afq	2016/01/27	57414	⋯ /1200	19.7	r	2018/01/28	58146	1200/200	14.12	*J*
	2017/02/15	57799	⋯ /1200	19.2	r	2019/12/02	58819	400/220	9.73	*K*
PV Cep	2015/06/24	57197	1200/1200	16.34	g	2016/12/08	57730	1200/240	9.06	*J*
V350 Cep	2019/07/04	58668	2400/2400	15.68[2] (0)	r	2015/11/08	57334	800/480	11.78[3] (+6)	*H*
	2019/10/02	58758	2400/2400	15.60[2] (0)	r	2018/09/29	58390	800/⋯	12.96	*J*
	2019/10/17	58773	2400/2400	15.79[2] (−1)	r	⋯	⋯	⋯	⋯	⋯

Note.
[a] Photometry obtained in the indicated filter during the same night as spectroscopy. Exceptions are flagged (1 = ASA-SN; 2 = ZTF, 3 = Campo Imperatore Telescope, Italy) with the number of days before (−) or after (+) the spectroscopic observation in parentheses.

flat-fielding, sky background subtraction, and extraction of the one-dimensional spectrum by integrating the stellar trace along the spatial direction. In the optical range, few telluric features are present, the most prominent being that around 7600 Å, around which, however, there are no lines used for the subsequent accretion and ejection analysis. Therefore, we have not applied any telluric correction to the optical spectra. Wavelength calibration was obtained from arc lamps. Intercalibration between blue and red spectral segments was verified superposing the spectral range between 5300 and 5900 Å in common between the two channels. In all cases, the Blue and Red spectra resulted optimally aligned without the need for further corrections.

The raw LUCI spectral images were flat-fielded, sky-subtracted, and corrected for optical distortions in both the spatial and spectral directions. Telluric absorptions were

removed using the normalized spectrum of a telluric standard star, after the removal of its intrinsic spectral features. Wavelength calibration was obtained from arc lamps spectra. In a few cases, we applied an intercalibration correction to align the *zJ* and *HK* segments, which did not exceeded 20% of the flux density.

The bad atmospheric conditions prevented us from flux calibrating the spectra by using spectrophotometric standards. Therefore, we used as absolute calibrators the acquisition images obtained immediately before the spectral images in the filter specified in Table 4. Photometry was obtained by taking as reference all the visible stars in the field, for which either a PAN-STARRS[16] (in the optical) or a 2MASS[17] (in the near-IR) photometry is available. In few cases, namely when not enough reference sources were present in the acquisition image or our target appeared saturated, we used the photometry retrieved from public databases and obtained a few days before or after the LBT observation (as specified in the note of Table 4).

4. Light Curves

To establish the level of accretion activity of each target at the time of the LBT observation we collected data from public surveys (ZTF, ASASSN, and AAVSO[18]) to derive the optical light curves of the sources over several years, which are displayed in Figure 1. For NY Ori and V1647 Ori, only the light curves of the ASASSN survey are available. Unfortunately, the ASASSN images of these sources are strongly contaminated by the diffuse emission of the ONC and Mc Neil's nebulae, where NY Ori and V1647 Ori are respectively located (Aspin et al. 2009; Herbig 2008). Therefore, these two light curves are not shown.

In the following, we briefly comment on the light curves of the remaining nine objects.

1. XZ Tau. The *V* band magnitude varied between ∼14.5 and 12 mag within a 6 yr period. Our MODS spectra cover both a high- and low-level brightness state.
2. UZ Tau E. This source shows a very small amplitude level of variability within 5 yr. It has maintained an average brightness level around $V = 12.7$ mag, with fluctuations of ∼0.3 mag. The spectroscopic observations were obtained at photometric levels with 0.6 mag of difference.
3. VY Tau. A remarkable brightening occurred at the beginning of 2014, unfortunately not covered by our observations. This was followed by a second low-amplitude burst about a year later. The first MODS spectrum refers to the declining phase of this burst.
4. V1143 Ori. Between 2013 and 2018 the source has remained at $V \sim 17$ mag with typical fluctuations of tenths of magnitude. The MODS spectrum was acquired at $V \sim 16.5$ mag.
5. DR Tau. In the last seven years, the DR Tau average photometry has been $V \sim 12$ mag, with large fluctuations up to 1 mag. All our observations have been performed close to the average level.
6. ASASSN-13db. This source underwent a first, short-lived outburst in 2013, followed by a second, more intense outburst from 2014 to late 2016. We have observed ASASSN-13db four times, the first three (two with MODS and one with LUCI) during the second burst and the last with MODS in 2017, when the source was back to quiescence.
7. iPTF15afq. The source underwent an outburst at the beginning of 2018 (not shown in the *r*-band light curve, see Hillenbrand 2019), followed by a quiescence period of about 2 years. A second outburst occurred in 2019, covered by our LUCI observation during the rising phase and close to the peak. A slow decay started at the beginning of 2020 and is still ongoing. The remaining three observations (between 2016 and 2018), have been taken during quiescence ($R \sim 18.5$–19 mag), according to the light curve presented by Miller et al. (2015).
8. PV Cep. Between 2013 and 2020, PV Cep has experienced a slow increase in brightness, with a peak in 2016 ($V \sim 14.5$ mag), followed by a decrease down to $V > 18$ mag at a roughly similar speed. Both our observations were conducted close to the brightness peak.
9. V350 Cep. Our first LUCI observation was taken in November 2015, at $R = 15.4$ mag (Semkov et al. 2017). The source experienced a deep dimming in spring 2016 followed by a new brightening. Since 2018, V350 Cep is again progressively and slowly fading (from $r \sim 15.3$ to $r \sim 15.8$). Our second LUCI observation (2018) was obtained when V350 Cep was still relatively bright ($r \sim 15.5$ mag), while the next three MODS spectra were taken when *r* had decreased down to 15.6–15.8 mag.

Summarizing, our targets have shown a variety of behaviors during the last decade. Some of them have remained fairly constant, others have undergone strong outbursts or long-term and remarkable brightness variations. As expected, in most cases, our observations were performed during phases of quiescence. However, some exceptions exist: we have observed XZ Tau and PV Cep during a high level of their activity and even caught the outbursts of ASASSN-13db and iPTF15afq. In addition, our acquisition images of NY Ori indicate a variation of about two magnitudes in the *r*-band between 2014 ($r \sim 12$) and 2016 ($r \sim 14$).

5. Description of the Spectra

Figures 2–3 and Figures 4–5 show the MODS and LUCI spectra of our sample, respectively. Line fluxes have been derived by fitting the profiles with a Gaussian function, and the relative uncertainties have been estimated by multiplying the rms noise of the continuum close to the line times the FWHM. Appendix A (Tables 8–18) report the fluxes of lines used in the analysis.

Lines tracing accretion have been detected in all sources. In particular, the Balmer recombination lines (typically from Hα to Hδ, but for many sources up to H15) are detected in all MODS spectra. In several objects (NY Ori, DR Tau, ASASSN-13db, V1647 Ori, PV Cep) some of these lines are partially or totally seen in absorption. Note that, given the late spectral type of the sources (Table 3), the photospheric contribution to the lines seen in absorption is negligible, with the possible exceptions of NY Ori and PV Cep. Paschen and Brackett lines (both in the optical and in near-IR range) are detected in 10 and 5 objects, respectively, and appear all in emission. In all objects observed with LUCI, we detect the He I 1.08 μm line, while other He I optical lines are seen in the spectra of the brightest objects. Metallic lines of many species (Fe I, Fe II, Ti I, Ti II, Ca II, Cr I, Cr II) are also detected.

[16] panstarss.stsci.edu
[17] ipach.caltech.edu/project/2mass
[18] https://www.aavso.org/

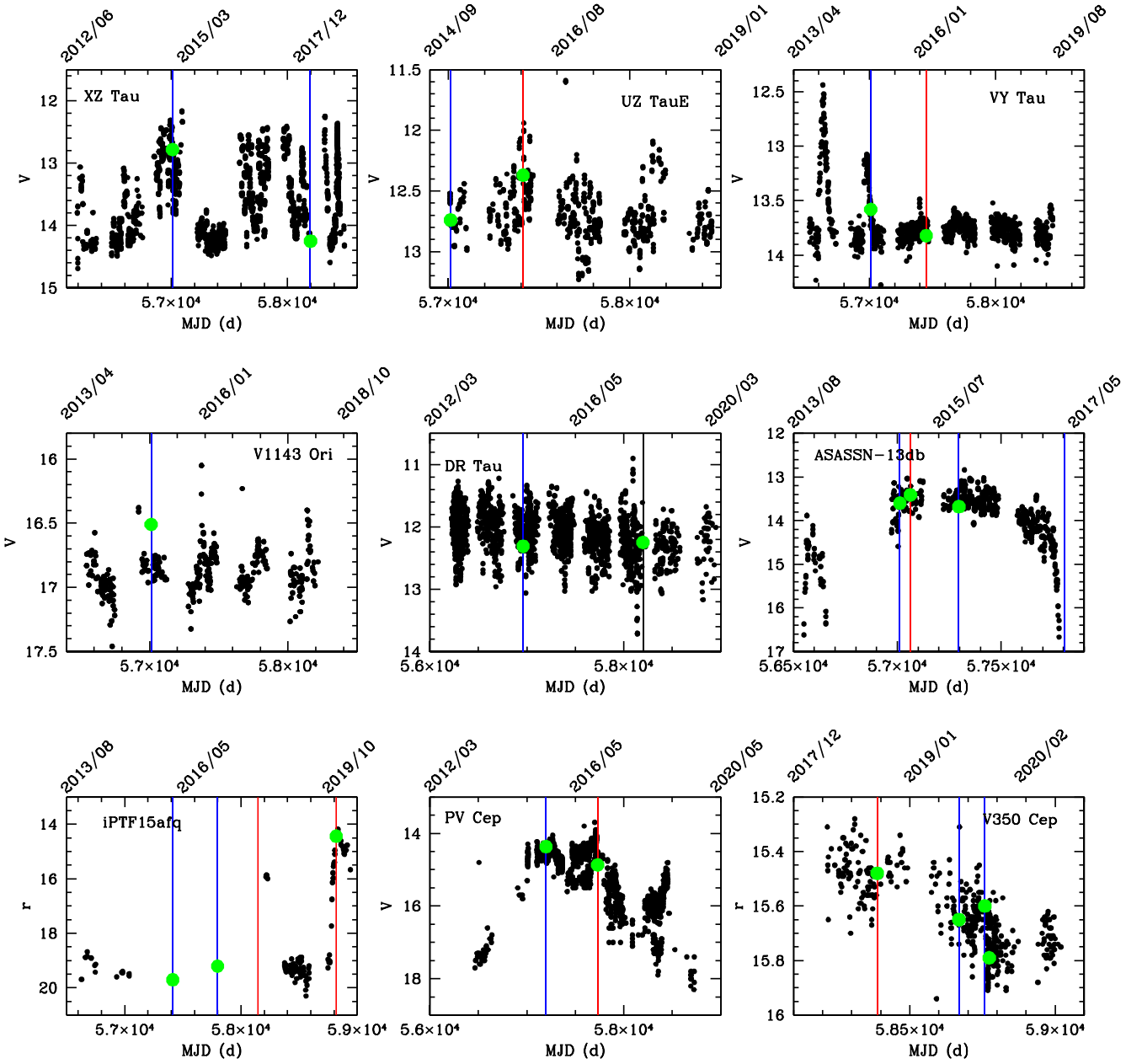

Figure 1. Optical (*V*- or *r*-band) light curves retrieved from data of public surveys (ZTF, ASASSN, and AAVSO). The *x*-axis represents the Modified Julian Date (MJD), while some calendar dates are given on top as reference. A blue (red) vertical line indicates the date of a MODS (LUCI) observation. The black line corresponds to quasi-simultaneous MODS+LUCI observation of DR Tau. Photometry taken closest in time to the spectroscopic observation is marked with a green dot.

Signatures of ejection activity, such as the [O I] 6300 Å line, are present in all sources but VY Tau and V1143 Ori. In two objects (iPTF15afq and V350 Cep), we also detected H_2 emission at 2.12 μm, which is a typical tracer of molecular outflows. In XZ Tau, UZ Tau E, DR Tau, and PV Cep, we detect some [S II] lines, indicative of gas with a low ionization degree. Lines of [S II], [Fe II], [Ni II], and [N II] have been detected in the spectrum of iPTF15afq, which could signal the occurrence of a high-velocity jet (Giannini et al. 2019).

In some of the LUCI spectra we have identified at least one of the two CO rovibrational band heads ($v = 2$-0 and $v = 3$-1) in emission (UZ Tau E, iPTF15afq, and PV Cep), or in absorption (VY Tau), as expected for EXor sources (e.g., Biscaya et al. 1997; Hillenbrand et al. 2013). In the remaining objects, the CO band heads are undetected, probably because the edge of the HK spectra is typically very noisy.

In general, we remark that (1) the spectra well resemble the optical/near-IR spectra of accreting T Tauri stars (e.g., Alcalá et al. 2017) and no evident differences exist among the spectra of known EXors and EXor candidates; (2) the intensity of the accretion tracers (e.g., H I, Ca II) follows the variation of the source brightness (e.g., XZ Tau, Table 8) and may even disappear or change from emission to absorption in case of an outburst event (ASASSN-13db and iPTF15afq).

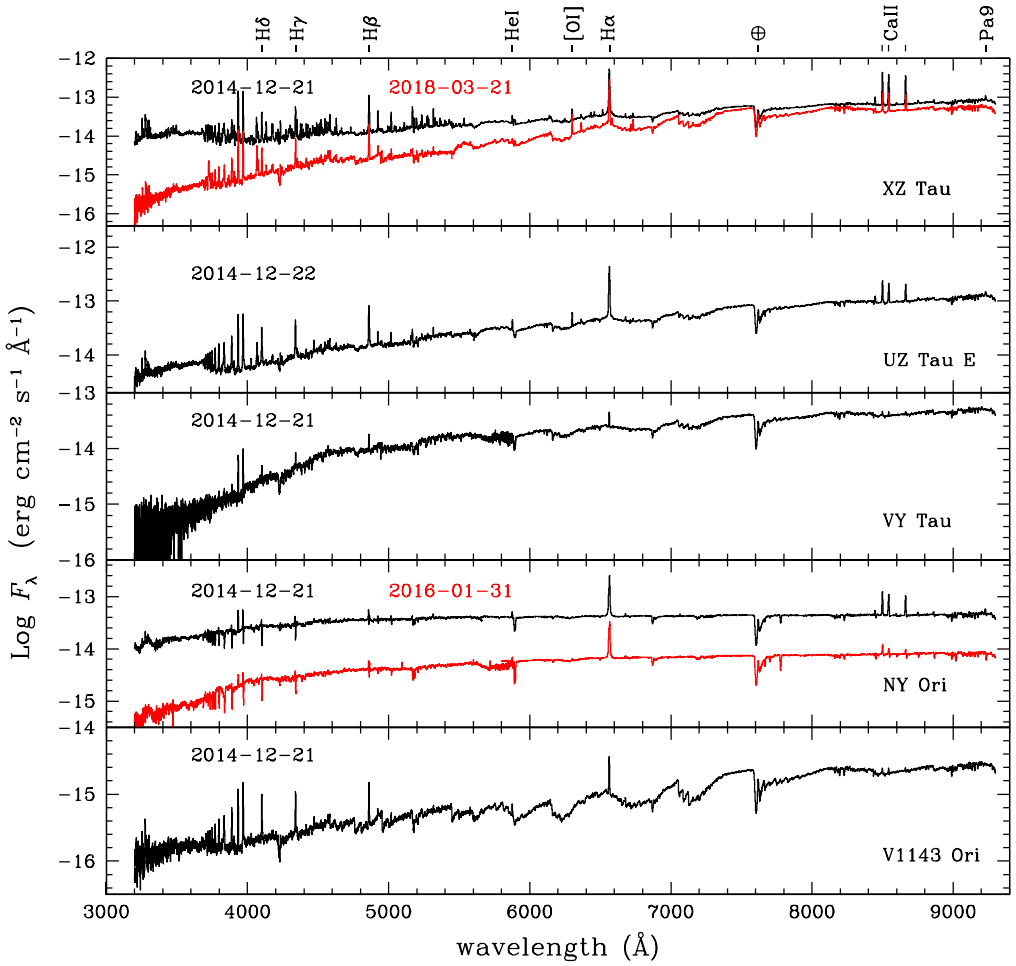

Figure 2. MODS spectra. Spectra obtained in different dates are shown with different colors. Brightest lines and telluric features are labeled.

6. Analysis and Discussion

6.1. Extinction

The primary goal of the present work is to determine the accretion parameters ($L_{\rm acc}$ and $\dot{M}_{\rm acc}$) of the sample. To get a meaningful estimate of these two quantities, we first derived the visual extinction ($A_{\rm V}$) toward the sources. As listed in Table 3, one or more $A_{\rm V}$ values are reported in the literature for some of them. Although these values represent an important reference, several studies have shown that a remarkable reduction (e.g., Hillenbrand et al. 2013), or less often, an increase of the extinction (in edge-on disks, Stock et al. 2020) often accompany accretion burst episodes. Therefore, we cannot assume $A_{\rm V}$ as a constant, but we need to estimate its value for each observation date. In the following, we separately discuss the methods used to derive $A_{\rm V}$ from both the optical and near-IR spectra.

6.1.1. Extinction Derived from Optical Spectra

The method used to derive the extinction from the optical spectra is described in detail in Giannini et al. (2018). This is essentially based on the empirical relationships found by Alcalá et al. (2014, 2017), between the accretion luminosity, $L_{\rm acc}$, and the luminosities $L_{\rm i}$ of selected emission lines (so-called "line method"). In the optical range these relationships exist for more than 20 lines, namely the H I recombination lines of the Balmer and Paschen series from Hα to H15, and from Pa8 to Pa10, along with He I, O I, and Ca II lines. Therefore, the relationships provide up to around 20 independent estimates of $L_{\rm acc}$, namely one for each observed line ($L_{\rm acc(i)}$).

In our procedure, we fit simultaneously $L_{\rm acc}$ and $A_{\rm V}$, this latter allowed to vary between 0 and 15 mag (in steps of 0.20 mag). The extinction law by Cardelli et al. (1989) and total-to-selective extinction ratio $R_{\rm V} = 3.1$ are assumed. We iteratively fit $L_{\rm acc}$ to minimize the dispersion among the individual $L_{\rm acc(i)}$, computed by de-reddening the observed fluxes for the current $A_{\rm V}$ and assuming the distance listed in Table 1. The best estimate of $A_{\rm V}$ is the value for which the dispersion between the $L_{\rm acc(i)}$ is minimized and we assume as $L_{\rm acc}$ the average of the $L_{\rm acc(i)}$ corresponding to that of $A_{\rm V}$.

We included in the fit only the lines that do not present any absorption component. We have verified that, rather than on the individual flux errors, the main limitation of this method comes from the uncertainties on the empirical relationships (Alcalá et al. 2017), which give an error on $A_{\rm V}$ of 0.5−1.5 mag, depending on how many lines are considered in the fit. Further causes of uncertainty come from the assumptions on the extinction law and $R_{\rm V}$. For example, we have checked that if the extinction law by Weingartner & Draine (2001) is applied, the fitted $A_{\rm V}$ decreases by ≈0.4 mag. Conversely, an increase in $A_{\rm V}$ by ∼0.2–0.3 mag is produced for $R_{\rm V} = 5.5$.

In Figures 6–8, we show the results of our procedure, while in Table 5, we report the fitted extinction values and the number of lines used.

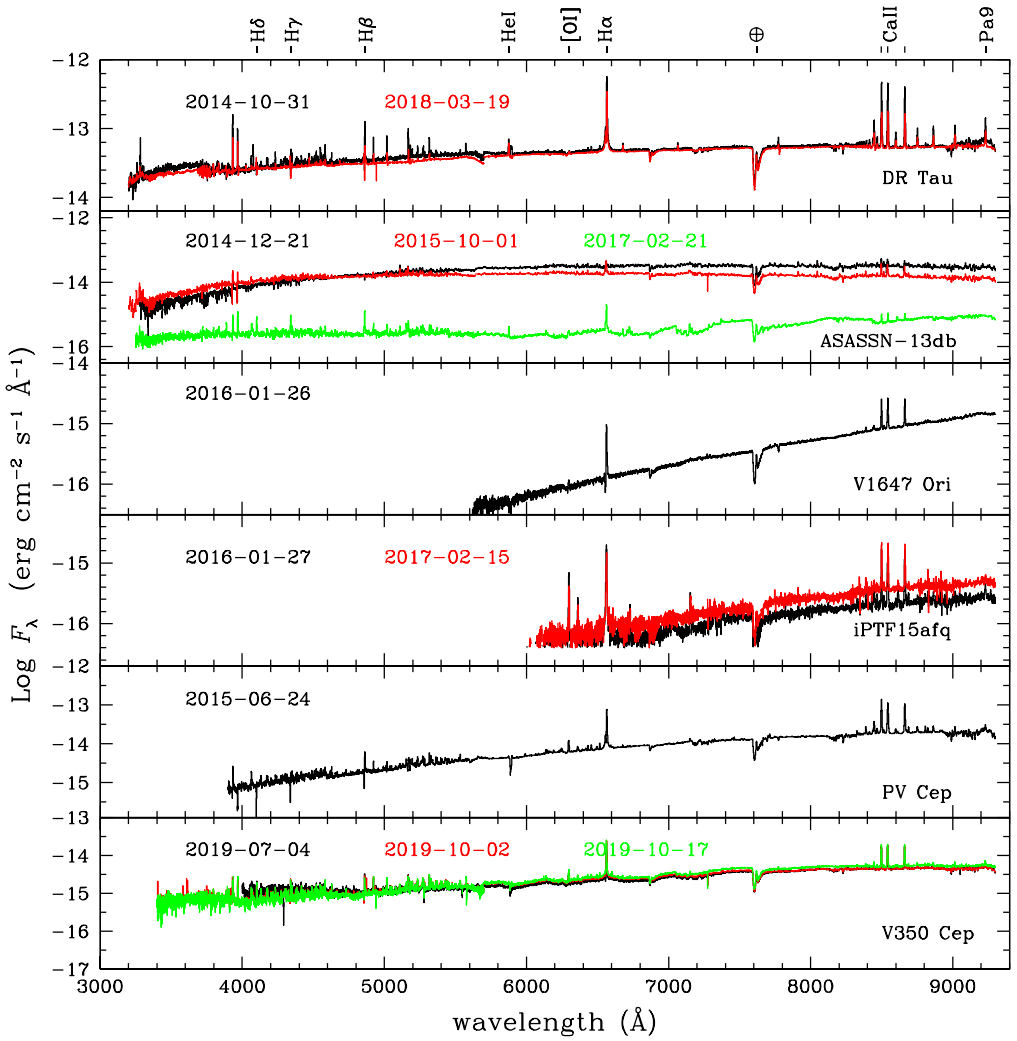

Figure 3. As in Figure 2.

An independent way to compute A_V has been described by Alcalá et al. (2021, so-called "continuum" method). The observed spectrum is iteratively divided by a template of the same spectral type (SpT), artificially reddened by varying the value of A_V. The best estimate of A_V is that for which the ratio has a flat slope. Applying this method to strong accretors, one has to correct the spectrum for the excess continuum (veiling) induced by the accretion hot spot (UV) and disk (IR) emission. This has been estimated for the majority of our sources by applying the procedure described in Appendix B.

Following the prescriptions by Alcalá et al. (2014) and Fischer et al. (2011), we applied the continuum method in the spectral range between 550 and 800 nm, where the veiling excess is minimized and expected not to change more than the typical error of 0.3 associated with its determination (Appendix B). We adopted as template spectra a grid of non-accreting (Class III) YSOs of the same SpT of the observed sources (Manara et al. 2013, 2017), reddened for A_V between 0 and 15 mag in steps of 0.20 mag. The results of the fitting procedure are provided in Figure 9 and the fitted A_V are listed in Table 5. Noticeably, in six out of the nine optical spectra examined, the two A_V determinations agree within 0.5 mag.

Finally, the case of V1647 Ori deserves a short discussion. This source is a well-known Class I/flat young source, still deeply embedded in the parental dusty envelope. As shown in several works (e.g., Nisini et al. 2016; Fiorellino et al. 2021), in embedded sources a relevant fraction of the optical emission originating close to the star is scattered in the cavity excavated inside the envelope. The effect is to enhance the emission at shorter wavelengths, that in turn simulates a lower extinction. For this reason, we consider the determination of A_V (9.2 mag) derived in the optical range to be not reliable and will assume the extinction derived from the LUCI spectrum on the same date (13 mag, Section 6.1.2).

6.1.2. Extinction Derived from Near-IR Spectra

The A_V estimate from the near-IR spectra was also obtained by applying two independent methods, briefly described in the following paragraph.

The first method is based on the [*J*-*H*] and [*H*-*K*] colors at the date of the observation. One photometric point is directly provided by the acquisition image (Table 4), while the other two are computed from the flux-calibrated spectrum convolved with the Johnson filter profiles.[19] We estimate that this procedure leads to an uncertainty of about ±0.1 mag in each band. From the magnitudes, we have constructed the [*J*-*H*]

[19] Retrived at http://svo2.cab.inta-csic.es/theory/fps/, Spanish Virtual Observatory (SVO) Filter Profile Service (Rodrigo & Solano 2020).

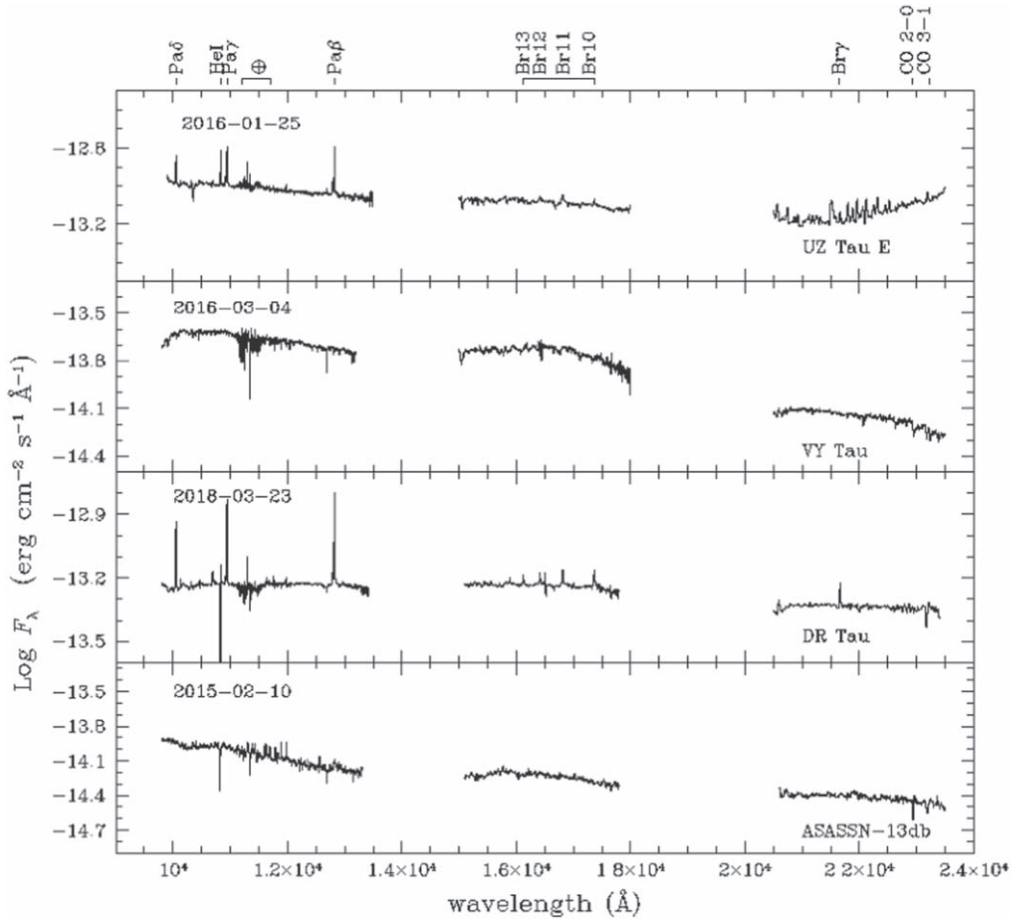

Figure 4. LUCI spectra. Spectra obtained in different dates are shown with different colors. Brightest lines are labeled.

versus [*H-K*] color–color diagram shown in Figure 10. Here, we indicate with an arrow the direction of the extinction vector, whose length corresponds to an extinction of 5 mag. We assume the reddening law by Cardelli et al. (1989) and $R_V = 3.1$. We estimate A_V from the position of the observed colors and the unreddened Classical T Tauri locus (CTTs, Meyer et al. 1997) and list the values in Table 5. Considering all the uncertainties involved in this procedure (absolute spectral calibration, propagation of magnitude errors, assumptions on extinction law and R_V), we conservatively evaluate a final error on A_V of 1 mag.

All sources have low or negligible A_V, with the exception of V1647 Ori ($A_V \sim 13$ mag). In the case of VY Tau, which is located at the left edge of Figure 10, we are not able to estimate a reliable value of A_V, while for two observations (iPTF15afq and V350 Cep) we cannot apply the method because the available spectra do not cover the three bands.

The second method relies on the detection of accretion line tracers, as done for the optical spectra, see Figures 6–8. However, empirical relationships in the near-IR are available only for the Paschen lines (from Pa8 to Pβ) and for the Brγ (Alcalá et al. 2017), which are moreover less sensitive to extinction variations than the optical lines. For DR Tau, for which we have quasi-simultaneous MODS and LUCI spectra, the optical and near-IR lines have been considered all together in the fit. Conversely, as explained in the previous section, the lines of V1647 Ori observed with LUCI have been fitted separately from those observed with MODS, although the two spectra were obtained on the same date. The fitted A_V of 13 mag is in perfect agreement with that derived from the color–color diagram.

We were able to apply both methods to five spectra. The two A_V determinations are in excellent agreement in UZ Tau E and V1647 Ori (Table 5), but differ between 0.9 and 3.3 mag in the other three sources (DR Tau, PV Cep, and V350 Cep). Since we have no reason to prefer one method over the other (also considering that the lines used in the fit of L_{acc} are few), we have assumed the entire range of A_V determinations to compute the accretion parameters L_{acc} and $\dot{M}_{acc}$ (see Section 6.2).

6.2. Accretion Luminosity and Mass Accretion Rate

As explained in Section 6.1.1, the accretion luminosity, L_{acc}, has been derived together with A_V by fitting the individual $L_{acc(i)}$. With reference to the fits shown in Figures 6–8 we note that, in general, the $L_{acc(i)}$ derived from the individual lines agree within the errors. There are however lines whose accretion luminosity may be up to an order of magnitude higher than the average L_{acc}. In particular, we signal Ca II K and He I at 492 and 502 nm. However, thanks to the high number of lines used, L_{acc} does not change by more than 10% whether or not these three lines are included in the fit.

For many sources, a further estimate of L_{acc} has been obtained by applying the relationships between L_{acc} and L_i by

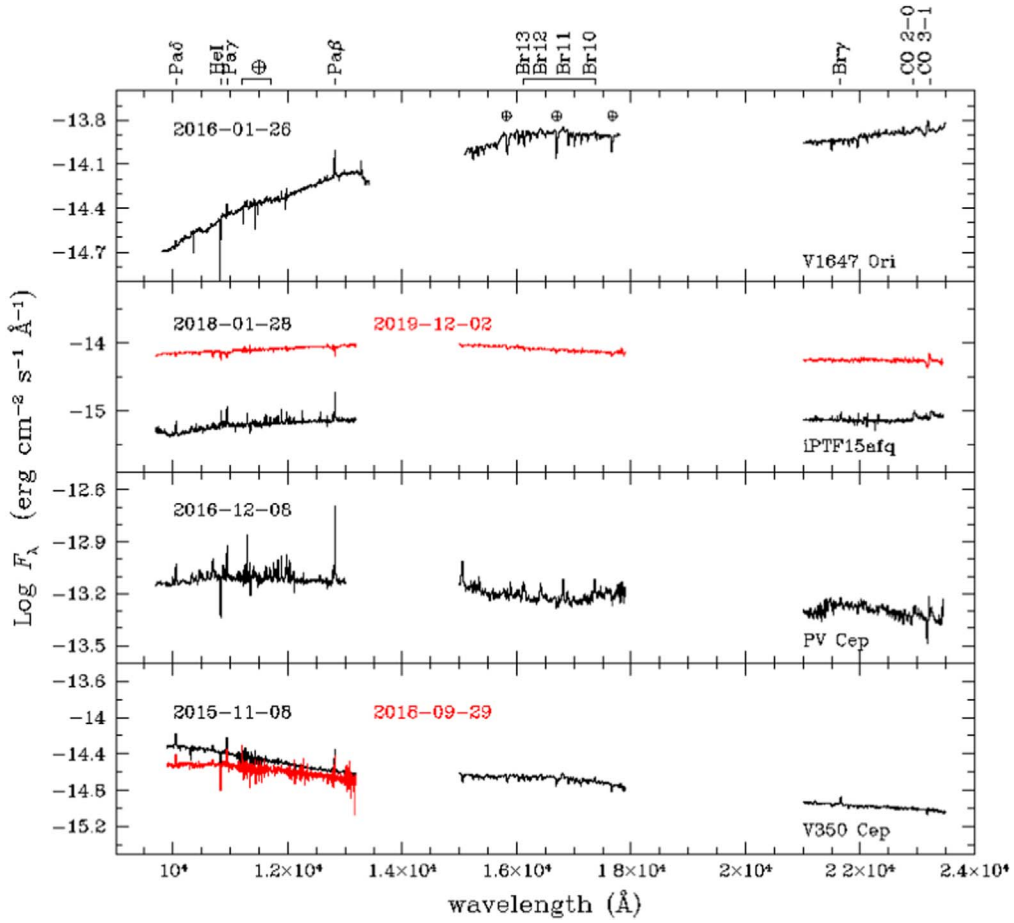

Figure 5. As in Figure 4.

fixing the A_V to the value derived by the continuum method (in the optical) or by the color–color diagram (in the infrared), see Table 6. This way, we have checked that L_{acc} does not change by more than 30%.

The mass accretion rate, $\dot{M}_{acc}$, has been estimated using the relationship by Gullbring et al. (1998):

$$\dot{M}_{acc} \approx 1.25 \frac{L_{acc} R_*}{G M_*} \quad (1)$$

where R_* and M_* are the stellar mass and radius, and G is the gravitational constant. We have adopted for M_* the values given in the literature (Table 3) and derived R_* from the relationship:

$$R_* = \frac{1}{2T_{eff}^2}\sqrt{\frac{L_*}{\pi\sigma}} \quad (2)$$

where σ is the Stefan-Boltzmann constant, and T_{eff} and L_* are taken from Table 3.

The derived $\dot{M}_{acc}$ values are listed in Table 6.

It is worth noting that no remarkable differences exist between EXors and EXor candidates, either in L_{acc} or in $\dot{M}_{acc}$. Typical values are $-2 \lesssim \mathrm{Log}(L_{acc}/L_\odot) \lesssim 1$, and $-9 \lesssim \mathrm{Log}(\dot{M}_{acc}/M_\odot\ \mathrm{yr}^{-1}) \lesssim -7$. V1647 Ori is the object with significantly higher $L_{acc}(\sim 50\, L_\odot)$ and $\dot{M}_{acc}$ ($\sim 2\ 10^{-5}\ M_\odot\ \mathrm{yr}^{-1}$), in line with its very young age and its classification as a Class I/flat source. This source underwent two outbursts during its recent history, one in 2003–2004 (Aspin et al. 2006) and another one in 2008–2011 (Aspin 2011). During the second outburst, its r-band photometry was ∼17.77 and $A_V = 8$ mag. In 2016, we measured $r = 18.68$, namely about 1 mag fainter. Despite that, our determination of $\dot{M}_{acc}$ is about one order of magnitude higher than the estimate of $(4 \pm 2)\ 10^{-6}\, M_\odot\ \mathrm{yr}^{-1}$ measured by Aspin (2011). This disagreement is due to the higher A_V (13 mag) that we have estimated from the LUCI spectrum. A considerable variability in A_V is indeed exhibited by V1647 Ori. During quiescence ($r \sim 23$), A_V was around 19 mag (Aspin 2011), therefore it is plausible to assume that in an intermediate stage, as that we have probed, also the extinction was in between the two extreme values of 8 and 19 mag. It would therefore be relevant to measure $\dot{M}_{acc}$ during the quiescent state (namely in the conditions of maximum A_V) to disentangle the contributions of accretion and extinction in the large-amplitude variability exhibited by this source.

The sources for which we have more than one observation are XZ Tau, UZ Tau E, NY Ori, DR Tau, ASASSN-13db, iPTF15afq, PV Cep, and V350 Cep. Of these, all but NY Ori and ASASSN-13db present an amplitude variability $\lesssim$1 mag (Figure 1), in line with that observed in Classical T Tauri stars (Costigan et al. 2014). These magnitude fluctuations correspond to variations in L_{acc} and $\dot{M}_{acc}$ of a factor ≈1.5−3. In general, these results confirm the accepted scenario in which accretion is a non-stationary phenomenon, although they are insufficient to explain the spread of more than two orders of

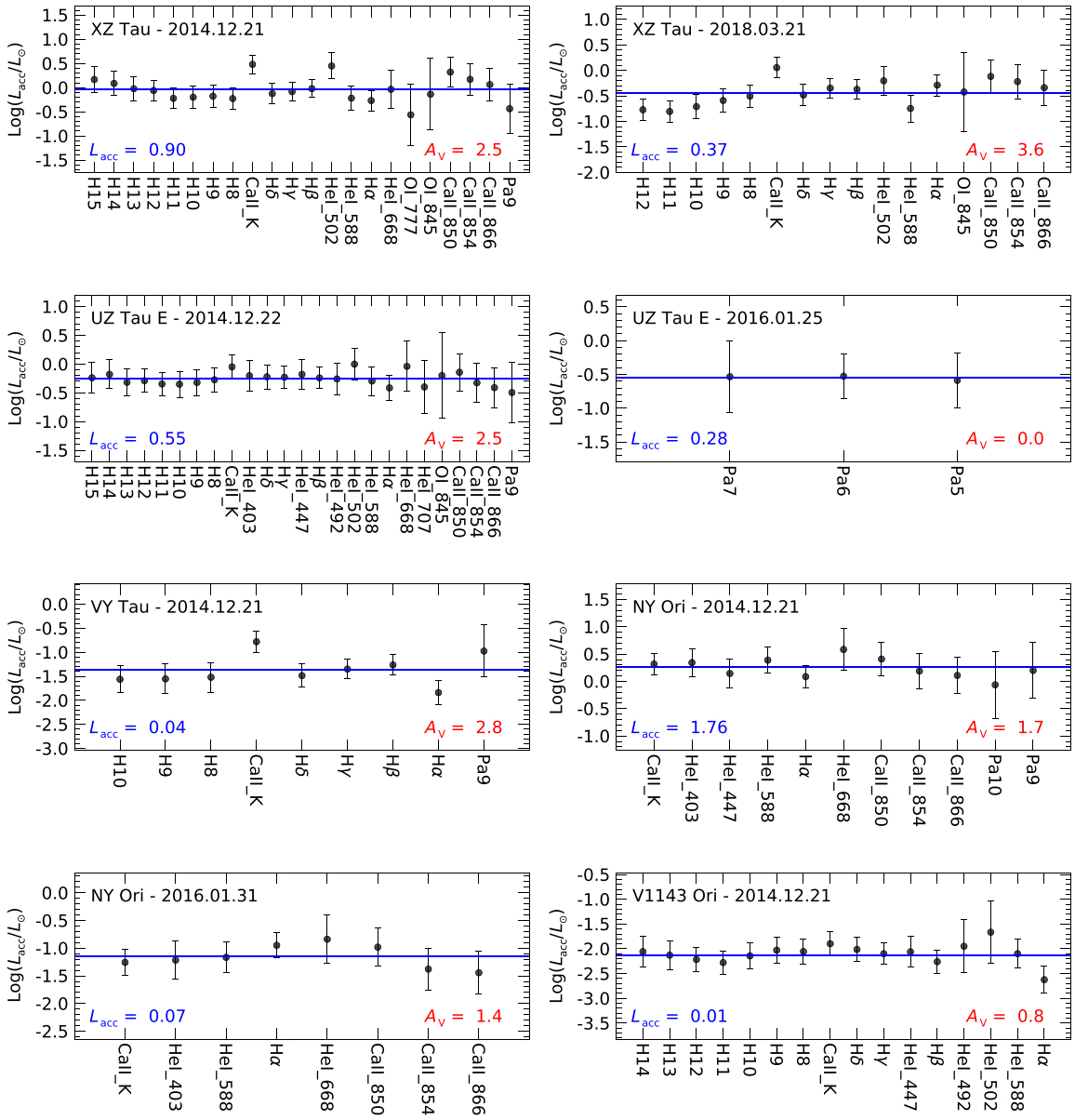

Figure 6. Accretion luminosity derived from the flux of the indicated tracers by using the relationships by Alcalá et al. (2017). The horizontal line shows the average L_{acc}. The source name, the observation date, and the fitted values of L_{acc}, and A_V are indicated.

magnitude found in the $\dot{M}_{acc}$ determinations among sources of the same mass (e.g., Antoniucci et al. 2014).

However, larger magnitude fluctuations imply significant variations in L_{acc} and $\dot{M}_{acc}$. In ASASSN-13b, in the two years between the outburst peak and the quiescence, L_{acc} changed from 0.2 to 0.03 $L_\odot$ and $\dot{M}_{acc}$ from 3 10^{-8} to 5 10^{-10} $M_\odot$ yr^{-1}. Also, in NY Ori L_{acc} decreased by a factor 25 in about one year (2014 December—2016 January). Although no photometric measurements are available for the indicated period, this change in L_{acc} is compatible with the variation of around 3 mag observed several times in this source (see Table 2).

6.3. Physical Conditions of the H I Lines Emitting Region

High-resolution spectroscopic observations indicate that both the high-velocity stellar winds and the gas channeled from the disk onto the stellar surface contribute to the hydrogen line profiles (e.g., Folha & Emerson 2001; Antoniucci et al. 2017a; Moura et al. 2020). Although our low-resolution observations do not allow to kinematically separate these two gas components, we can evaluate the average physical conditions of the hydrogen lines emitting regions using the observed flux ratios as temperature and density diagnostics.

Using their local line-excitation model, Kwan & Fischer (2011) provided predictions of the Balmer decrements (ratios from H15 to Hα with respect to Hβ), in the range of hydrogen density $8 \leqslant \log[n_H(\mathrm{cm}^{-3})] \leqslant 12$, and temperature between 3750 K and 15,000 K. Similarly, Paschen decrements (ratios from Paγ to Pa12 with respect to Paβ), together with the ratio Br10/Brγ are given by Edwards et al. (2013) for $8 \leqslant \log[n_H(\mathrm{cm}^{-3})] \leqslant 12.4$ and $T = 5000-20{,}000$ K.

Fits through the intrinsic hydrogen line fluxes have been done by least squares method for sources where at least four

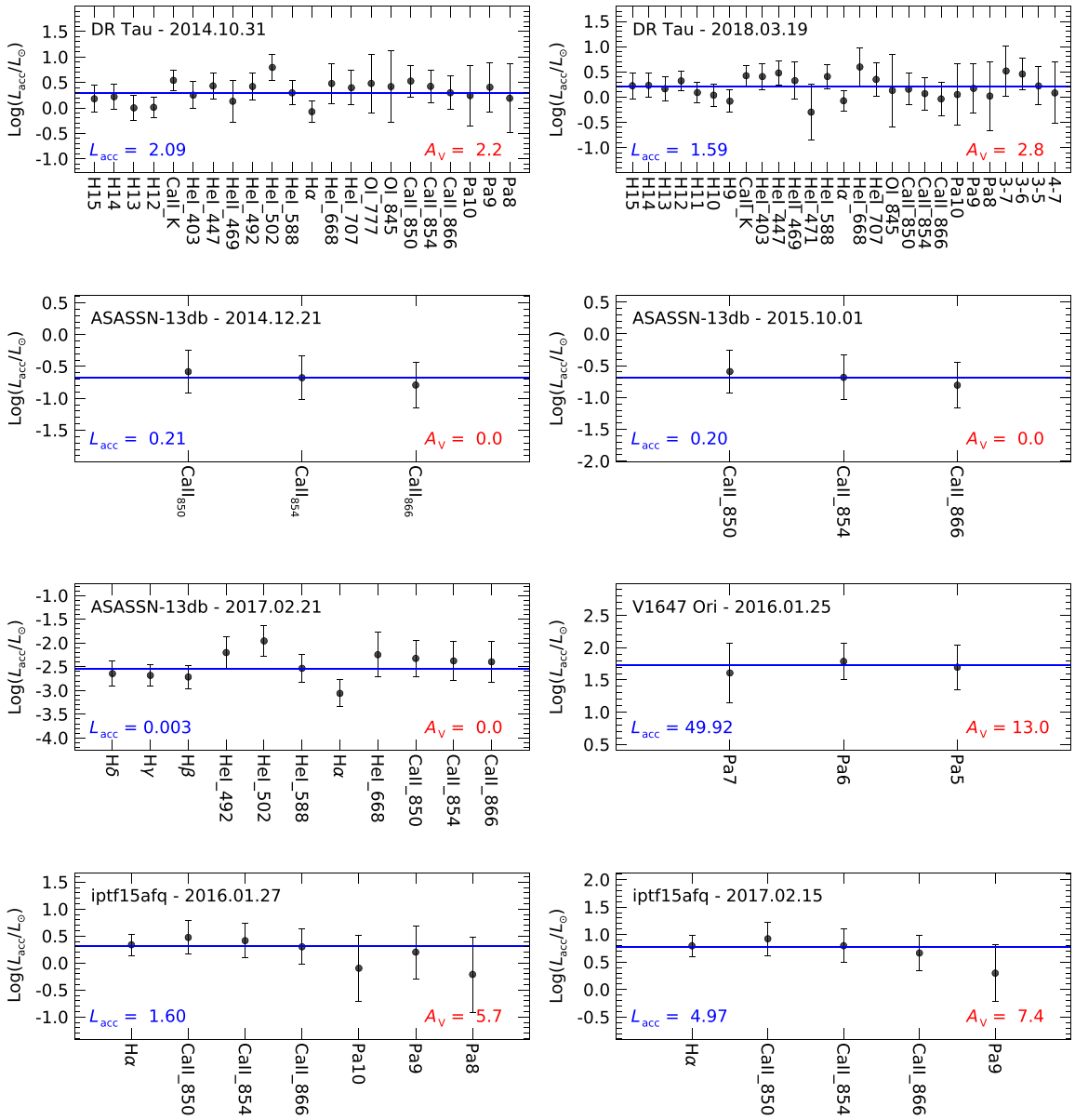

Figure 7. As in Figure 6.

lines are detected. As an example, we show in Figure 11 the Balmer decrement measured in XZ Tau for the two observation dates (2014 and 2018). We plotted the $H_i/H\beta$ ratios up to H14/$H\beta$ and H12/$H\beta$ for the 2014 (black) and 2018 (red) observations, respectively. First, we note the different shape of the Balmer decrement in the two dates. Following the nomenclature of Antoniucci et al. (2017b), in 2014 the decrement shape was of "type 4", typical of strong accretors, and changed in 2018 to the "type 2" shape, which is the one most frequently seen in T Tauri stars. This shape can be explained by variation of a factor ∼2.5 in n_H, with ratios $H_i/H\beta$ increasing with n_{up} in models with higher densities. Conversely, no clear correlation is found between the temperature and the shape of the Balmer decrement, and in particular, all the temperatures considered in the Kwan & Fischer model are compatible for the observation in 2018.

Table 7 summarizes the results for the objects of our sample, also reporting the brightness level of each source as derived from the photometric data and the number of lines involved in the fit. As pointed out for the case of XZ Tau, the temperature is not well constrained, apart from the case of UZ Tau E. It is therefore more interesting to focus on the results regarding the hydrogen density. In our previous study on the 2015 outburst of the classical EXor V1118 Ori, we highlighted the sudden increase in the hydrogen density of about two orders of magnitude, from $\log(n_H) = 9.4$ to $\log(n_H) = 11.4$, passing from the quiescent phase to the peak of the outburst (Giannini et al. 2017). In the objects of the sample presented here, we fit the hydrogen density in the range $\log(n_H)$ from 9.0 to 11.0, considering the uncertainties. Indeed, a certain level of correlation may be found between n_H and the activity level of the source. In Section 4 and 6.2, we identified XZ Tau, PV Cep, iPTF15afq, ASASSN-13db, and NY Ori as sources that showed considerable photometric variability during the last years, often accompanied by a significant L_{acc} and $\dot{M}_{acc}$ variations. Specifically, in XZ Tau the V band magnitude

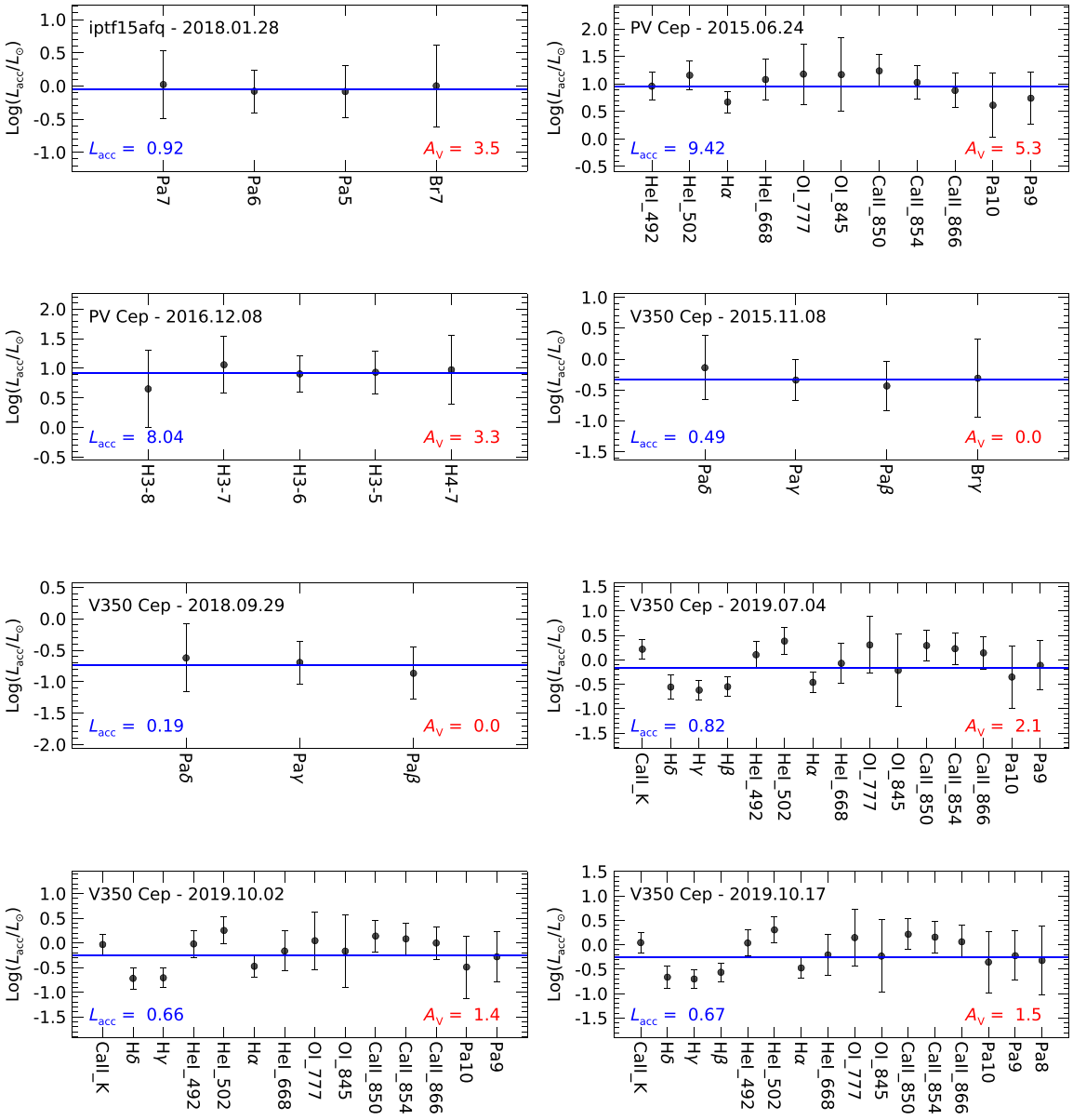

Figure 8. As in Figure 6.

increased from $V \sim 12.8$ in 2014 to $V \sim 14.2$ in 2018. Our analysis shows that this resulted in a decrease of veiling from 0.8 to 0.0, of $\dot{M}_{acc}$ by a factor of 5 and of n_H by a factor around 2.5–3.0. PV Cep has been observed only during a period of high brightness. Close to the peak of the light curve in 2015, we fit $\log(n_H) = 11.0$. In ASASSN-13db and in iPTF15afq, we are able to measure n_H only during the quiescent phase. It is interesting to note, however, that during periods of high brightness level (2014–2015 for ASASSN-13db and 2019 for iPTF15afq), the H I lines are always seen in absorption, a signature typical of FUors or in general of sources with a high accretion rate (Connelley & Reipurth 2018). In NY Ori the situation is more controversial. From our acquisition images, we find differences of about two magnitudes in the *r*-band between 2014 ($r \sim 12$) and 2016 ($r \sim 14$). All H I lines (from the Balmer and Paschen series) are seen in absorption in 2016, while the Paschen lines are in emission in 2014. Given the spectral type of NY Ori (K4), a possibility is that during quiescence the observed H I lines are in absorption because they originate in the photosphere, while during outburst the accretion component in emission dominates.

In the remaining sources, which are all observed during quiescence, $\log(n_H)$ is typically between 9.0 and 10.0. Only in V350 Cep we estimate $\log(n_H)$ between 10.6 and 10.8 in 2015. Unfortunatly, the photometric level at that date is unknown.

6.4. Mass Loss Variability and Forbidden Line Emission

Matter accretion from a disk necessarily imposes the removal of angular momentum through winds and jets. This makes the phenomena of mass accretion and ejection intimately correlated, so it is interesting to investigate whether they are also connected in terms of variability.

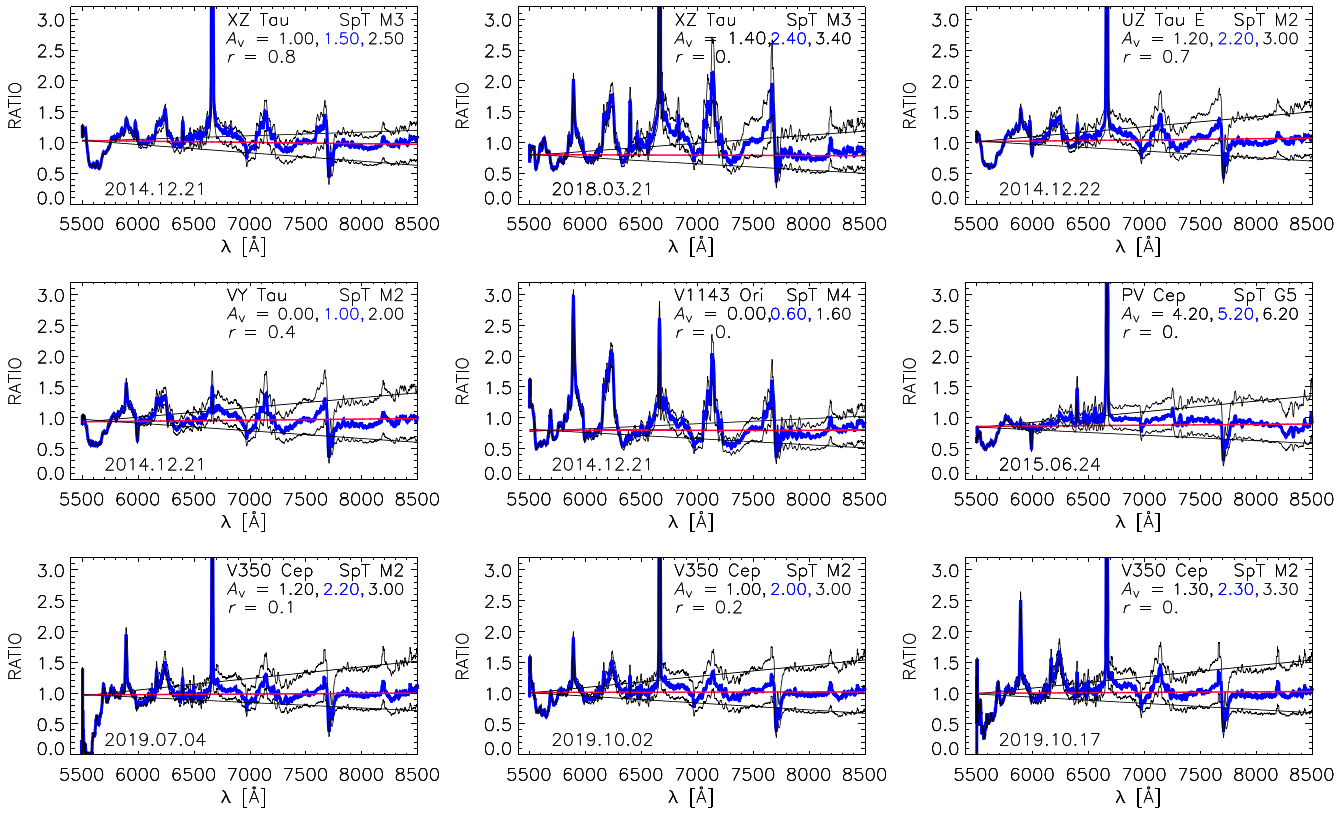

Figure 9. Ratios between observed spectra and artificially reddened and veiling-corrected templates. Ratios with minimum slopes (for which the extinction A_V is estimated) are indicated in blue. For each panel, object name, date of observation, spectral type, and veiling are also reported.

Table 5
A_V, and Veiling Derived from Optical and Near-infrared Spectra

Source	Optical					Near-infrared			
	Date	Continuum		Lines		Date	Col–Col	Lines	
		r_{710}[a]	A_V	N_l	A_V		A_V	N_l	A_V
	(yy/mm/dd)		(mag)		(mag)	(yy/mm/dd)	(mag)		(mag)
XZ Tau	2014/12/21	0.8	1.0–2.0	22	2.0–3.0	…	…	…	…
	2018/03/21	0.0	1.4–3.4	16	2.8–4.4	…	…	…	…
UZ Tau E	2014/12/22	0.7	1.6–3.0	25	2.0–3.0	2016/01/25	0.0–1.5	3	0.0–1.5
VY Tau	2014/12/21	0.4	0.0–2.0	9	1.6–4.0	2016/03/04	…	0	…
NY Ori	2014/12/21	0.2[b]	…	11	0.4–2.4	…	…	…	…
	2016/01/31	0.1[b]	…	8	0.5–2.9	…	…	…	…
V1143 Ori	2014/12/21	0.0	0.0–1.2	16	0.0–1.6	…	…	…	…
DR Tau	2014/10/31	>0.5[b]	…	22	1.7–2.6	2018/03/23	0.5[b]–2.5	27[c]	2.0–2.9
	2018/03/19	>0.5[b]	…	27[c]	2.0–2.9	…	…	…	…
ASASSN-13db	2014/12/21	>3	…	3	0.0–1.5	2015/02/10	0.0–1.5	1	…
	2015/10/01	>3	…	3	0.0–1.5	…	…	…	…
	2017/02/21	0.4	0.0–0.2	11	0.0–1.0	…	…	…	…
V1647 Ori	2016/01/26	>2.5	…	5	7.7–10.6	2016/01/26	12.0–14.0	3	12.0–14.0
iPTF15afq	2016/01/27	…	…	7	4.2–7.7	2018/01/28	…	4	2.0-5.0
	2017/02/15	…	…	5	5.9–8.9	2019/12/02	0.3–2.3	0	…
PV Cep	2015/06/24	0.0[b]	…	11	4.3–6.3	2016/12/08	0.0–1.0	5	1.8–5.1
V350 Cep	2019/07/04	0.1	1.4–3.0	15	1.3–2.9	2015/11/08	0.8–2.8	4	0.0–1.5
	2019/10/02	0.2	1.0–3.0	14	0.6–2.2	2018/09/29	…	3	0.0–1.5
	2019/10/17	0.0	1.3–3.3	16	0.7–2.3	…	…	…	…

Notes.
[a] Typical error on r_{710} is 0.3 (Appendix B).
[b] Derived by assuming the A_V value fitted from the accretion lines (see Appendix B for more details).
[c] Optical and near-infrared lines have been combined.

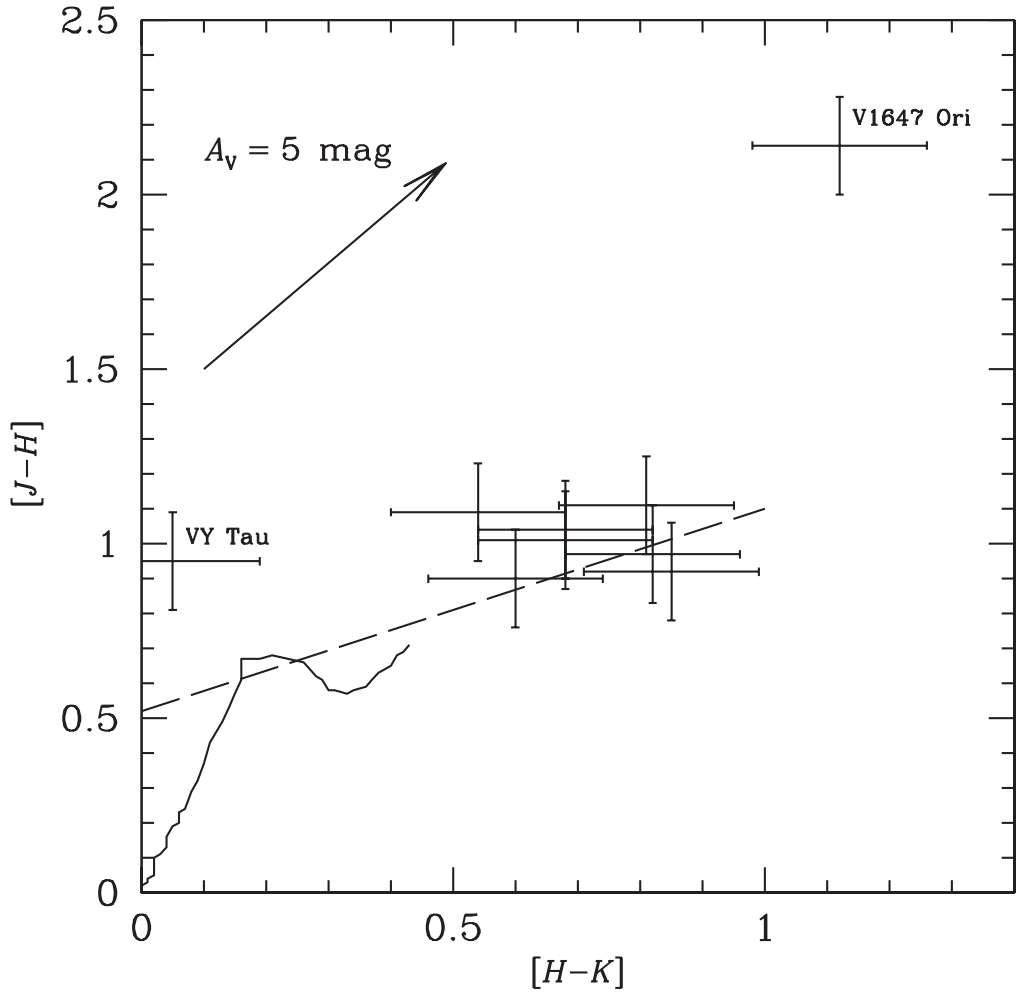

Figure 10. $[J-H]$ vs. $[H-K]$ color–color diagram. The arrow shows the extinction vector for $A_V = 5$ mag, according to the reddening law by Cardelli et al. (1989). The dashed line marks the *locus* of the unreddened T Tauri stars (Meyer et al. 1997), while the continuous line represents main sequence stars (Luhman et al. 2010). Data points of the objects discussed in the text are labeled.

Mass loss rate determinations suffer from multiple assumptions on the geometry and physical conditions of the outflowing gas (e.g., Sperling et al. 2020). Therefore, rather than searching for correlations between the rates of accretion and ejection, we have preferred to look for flux variations of lines representative of the two phenomena.

The [O I] 6300 Å is the most prominent outflow emission feature. Indeed, it was detected in all our objects but VY Tau and V1143 Ori, namely the two sources with the lowest values of $\dot{M}_{acc}$.

As tracer of accretion we have selected the Hα line, both because of its brightness and, more importantly, because the ratio Hα/[O I] 6300 Å, being independent of extinction, is directly related to the intrinsic ratio between mass accretion and mass ejection rates.

Among the five sources showing a significant $\dot{M}_{acc}$ variation, we have multi-epoch determinations of the [O I] 6300 Å for XZ Tau, NY Ori, and iPTF15afq. With reference to the line fluxes reported in Appendix A, we find that in XZ Tau F([O I] 6300 Å) has remained fairly constant while F(Hα) decreased by a factor ∼2.4 from 2014 to 2018. This indicates that between 2014 and 2018 the variation of the mass accretion has been significantly larger than that of the mass loss. Similarly, in NY Ori, F(Hα) and F([O I] 6300 Å) decreased by a factor of seven and three in two years (2014−2016). In iPTF15afq we observe the same trend although the variation is low for both lines, due to the short temporal distance of just one year.

More striking is the trend in the classical EXor V1118 Ori. Indeed, comparing the Hα and [O I] 6300 Å fluxes during the 2015 outburst (Giannini et al. 2016, 2017), with those of quiescence (Lorenzetti et al. 2015) we find a variation of F(Hα) about ten times larger than the variation of F([O I] 6300 Å).

7. Conclusions

We analyzed optical and near-IR low-resolution spectra taken at LBT between 2014 and 2019 of a sample of 11 variable young sources, composed of five well-known eruptive variables (EXors) and six pre-main-sequence objects showing episodic variability likely attributable to intermittent accretion events (EXor candidates). Ten sources have been observed more than once, therefore allowing us to investigate for correlations between photometric and spectroscopic variability. At this stage, the collected observations represent the first flux-limited spectroscopic survey of candidate eruptive variables able to accurately determining fundamental quantities such as visual extinction; accretion parameters; physical parameters of the H I lines emitting region, and signatures of mass

Table 6
Accretion Luminosity and Mass Accretion Rate

Source	Date (yy/mm/dd)	$L_{acc}/L_{\odot}$	$\log(\dot{M}_{acc}/M_{\odot}\ yr^{-1})$
XZ Tau	2014/12/21	0.30–0.90	−7.16−−6.68
	2018/03/21	0.10–0.37	−7.06−−7.63
UZ Tau E	2014/12/22	0.40–0.55	−6.92−−6.78
	2016/01/25	0.28–0.50	−7.07−−6.83
VY Tau	2014/12/21	0.004–0.04	−9.13−−8.16
NY Ori	2014/12/21	0.60–3.60	⋯
	2016/01/31	0.03–0.33	⋯
V1143 Ori	2014/12/21	0.006–0.01	−9.23−−9.11
DR Tau	2014/10/31	1.31–3.40	−7.11−−6.69
	2018/03/19-23	0.70–1.74	−7.38−−6.98
ASASSN-13db	2014/12/21	0.21–0.41	−7.48−−7.17
	2015/02/10	0.11–0.14	−7.76−−7.64
	2015/10/01	0.20–0.41	−7.48−−7.18
	2017/02/21	0.003–0.009	−9.26−−8.85
V1647 Ori	2016/01/26	7.24–20.89	−5.72−−5.26
iPTF15afq	2016/01/27	0.72–3.54	⋯
	2017/02/15	2.18–11.20	⋯
	2018/01/28	0.58–1.47	⋯
PV Cep	2015/06/24	4.78–18.60	−6.54−−5.95
	2016/12/08	2.63–8.04	−6.79−−6.31
V350 Cep	2015/11/08	0.49–0.87	⋯
	2018/09/29	0.19–0.32	⋯
	2019/07/04	0.82–0.89	⋯
	2019/10/02	0.66–1.09	⋯
	2019/10/17	0.67–1.31	⋯

outflowing. The main results of this survey can be summarized as follows:

1. The analysis of the light curves indicates that six sources (UZ Tau E, VY Tau, V1143 Ori, DR Tau, V1647 Ori, and V350 Cep) have been observed while in quiescence and another two, XZ Tau, nd PV Cep, during a high level of brightness. Remarkably, ASASSN-13db and iPTF15afq have been caught during outburst.
2. All targets present lines that are tracers of accretion, like H I recombination lines, both in the optical and IR range. All IR spectra show prominent Ca II and He I 1.08 μm lines. Metallic lines of many species are also detected. Signatures of ejection activity ([O I] 6300 Å,[S II],H_2 2.12 μm) characterize about 80% of the sources. No evident difference exists between the spectra of known and candidate EXors, all of them resembling spectra of accreting young T Tauri stars.
3. For many sources the veiling excess was computed. We found that a significant variation of the veiling is associated with accretion events. During the 2015 outburst of ASASSN-13db the veiling at 710 nm increased from 0.1 to >3.
4. Since the visual extinction A_V closely depends on the source activity level at the time of the observation, a major effort has been made to accurately evaluate this parameter. For both optical and near-IR spectra, two independent methods (based on lines, continuum, and colors) were used to derive A_V values.
5. Empirical relationships between the accretion luminosity (L_{acc}) and the luminosity of selected lines allowed us to determine the average accretion luminosity for each source and date of observation. The mass accretion rate was also evaluated. We did not find any remarkable difference between the L_{acc} and $\dot{M}_{acc}$ values of known EXors and EXor candidates of our sample, which are in the range $-2 \lesssim \mathrm{Log}(L_{acc}/L_{\odot}) \lesssim 1$ and $-9 \lesssim \mathrm{Log}(\dot{M}_{acc}/M_{\odot}\ yr^{-1}) \lesssim -7$, respectively.
6. All sources observed more than once present significant $\dot{M}_{acc}$ variability even if they have been observed during quiescence. In ASASSN-13db, a decrease of $\dot{M}_{acc}$ of two orders of magnitude is observed from the outburst peak to the quiescent phase. Also, the accretion luminosity of NY Ori decreased by a factor 25 in one year.
7. Physical parameters (n_H and T) of the H I emitting region have been evaluated from the observed hydrogen line ratios by using predictions provided in the literature. These ratios are much more effective in constraining the density (n_H) than the temperature, which remains poorly defined. Generally, a direct correlation is recognizable between density and accretion activity of the source, with significant density increases (up to two orders of magnitudes) associated with large brightness fluctuations.
8. Tracers of mass outflows, such as the [O I] 6300 Å line, have been detected in most of the investigated sources. By comparing the [O I] variations with those of a mass accretion tracer (Hα), we conclude that mass accretion variations are larger than mass loss variations.

In the next future, other facilities appropriate for this research will be available in the southern hemisphere, which are expected both to discover large numbers of eruptive variables (e.g., VRO-LSST), and to spectroscopically follow them in the optical/near-IR band (e.g., SoXS at ESO-NTT). Their observations will

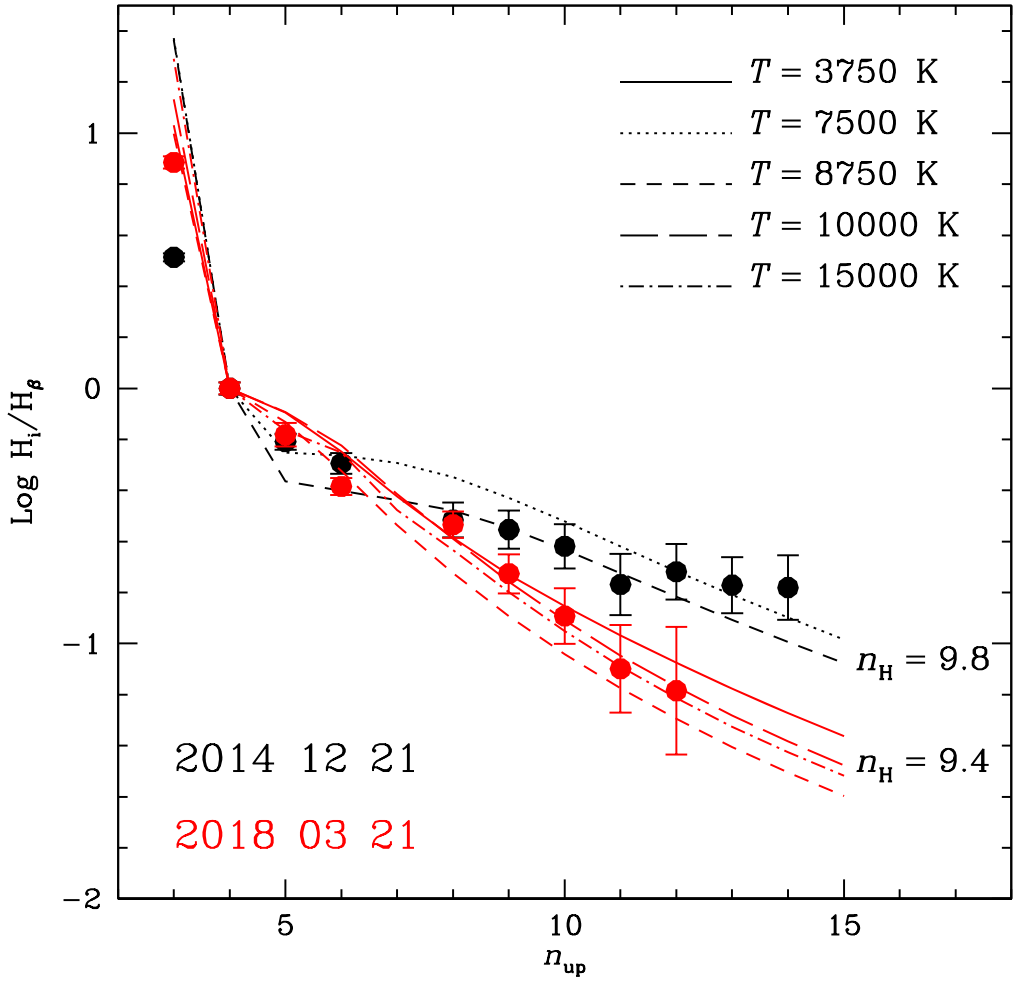

Figure 11. Balmer decrement ($H_i/H\beta$ flux ratios vs. upper level of the transition) of XZ Tau in the two dates of observation (black: 2014/12/21, red: 2018/03/21). The hydrogen density fitted for the two sets of data is reported in logarithmic scale. Different line symbols represent different temperatures as indicated in the top-right corner of the figure.

Table 7
Hydrogen Physical Parameters Derived from Balmer, Paschen, and Brackett Line Ratios

Source	Date (yy/mm/dd)	Bright. level	Series	N_{lines}	Log[n_H(cm^{-3})]	T (K)
XZ Tau	2014/12/21	H	Ba	11	9.8	7500–8750
	2018/03/21	L	Ba	9	9.4	all
UZ Tau E	2014/12/22	L	Ba	11	9.8	7500–8750
	2016/01/25	I	Pa+Br	4	10.6–10.8	5000–12,500
VY Tau	2014/12/21	L	Ba	7	9.2–9.4	all
NY Ori	2014/12/21	H	Pa	4	9.0–10.4	5000–12500
V1143 Ori	2014/12/21	I	Ba	11	9.2–9.4	all
DR Tau	2014/10/31	L	Ba+Pa	9	10.0–10.8	5000-12,500
	2018/03/19-23	L	Ba+Pa+Br	20	10.6–11.0	8750-12,500
ASASSN-13db	2017/02/21	L	Ba	5	9.4	all
V1647 Ori	2016/01/26	?	Ba+Pa	4	9.0–10.0	8750–12,500
iPTF15afq	2016/01/27	L?	Pa	5	9.0–10.6	all
	2018/01/28	L?	Pa+Br	4	10.4–11.0	all
PV Cep	2015/06/24	H	Pa	4	11.0	8750–12,500
	2016/12/08	H	Pa+Br	6	9.0–10.4	all
V350 Cep	2015/11/08	I	Pa+Br	5	10.6–10.8	all
	2019/07/04	I	Ba+Pa	8	9.2–9.8	all
	2019/10/02	I	Ba+Pa	8	9.2–9.8	all
	2019/10/17	I	Ba+Pa	8	9.2–9.8	all

Note.
[a] Brightness level as retrieved from photometric data. H, high; I, intermediate; L, low.

probably deeply modify our knowledge of the eruptive accretion phenomenon. In such a framework, we hope that our coherent database will represent a valuable reference study.

This work is based on observations made with the Large Binocular Telescope (LBT). The LBT is an international collaboration among institutions in the United States, Italy, and Germany. LBT Corporation partners are The University of Arizona on behalf of the Arizona university system; Istituto Nazionale di Astrofisica, Italy; LBT Beteiligungsgesellschaft, Germany, representing the Max-Planck Society, the Astrophysical Institute Potsdam, and Heidelberg University; The Ohio State University, and The Research Corporation, on behalf of The University of Notre Dame, University of Minnesota, and University of Virginia. This work has been supported by the project PRIN-INAF-MAIN-STREAM 2017 "Protoplanetary disks seen through the eyes of new-generation instruments" and by the European Union's Horizon 2020 research and innovation program under the Marie Sklodowska-Curie grant agreement No 823823 (DUST-BUSTERS). We also acknowledge the support by INAF/Frontiera through the "Progetti Premiali" funding scheme of the Italian Ministry of Education, University, and Research and by the Deutsche Forschungs-Gemeinschaft (DFG, German Research Foundation) - Refno. FOR 26341/1 TE 1024/1-1. This research also received financial support from the project PRIN-INAF 2019 "Spectroscopically Tracing the Disk Dispersal Evolution". A.C. G. received funding from the European Research Council (ERC) under the European Union's Horizon 2020 research and innovation program (grant agreement No. 743029). A.R. acknowledges support from the INAF project Premiale Supporto Arizona & Italia. This work has made use of data from the European Space Agency (ESA) mission Gaia (https://www.cosmos.esa.int/gaia), processed by the Gaia Data Processing and Analysis Consortium (DPAC, https://www.cosmos.esa.int/web/gaia/dpac/consortium). Funding for the DPAC has been provided by national institutions, in particular the institutions participating in the Gaia Multilateral Agreement.

Appendix A

In this Appendix we give the Tables of the lines fluxes used in the analysis (Tables 8–18). We report the line identification and wavelength (air wavelength for optical lines (λ 1 μm)), along with the measured flux *cgs* units) for each date of observation.

Table 8
XZ Tau: Observed Lines

		2014/12/21	2018/03/21
Line	λ_{air} (Å)	$F \pm \Delta F$ (10^{-14} erg s^{-1} cm^{-2})	
H15	3711.977	3.2 ± 0.2	…
H14	3721.938	3.5 ± 0.2	…
H13	3734.368	3.6 ± 0.2	…
H12	3750.151	4.1 ± 0.2	0.18 ± 0.02
H11	3770.630	3.7 ± 0.2	0.22 ± 0.02
H10	3797.898	5.3 ± 0.2	0.36 ± 0.02
H9	3835.384	6.3 ± 0.3	0.55 ± 0.02
H8	3889.049	7.4 ± 0.2	0.88 ± 0.02
Ca II K	3933.660	51.3 ± 0.1	4.4 ± 0.02
Ca II H/H7	3968.470	47.9 ± 0.1	4.3 ± 0.02
Hδ	4101.702	13.8 ± 0.2	1.5 ± 0.02
Hγ	4340.464	20.4 ± 0.2	3.0 ± 0.05
Hβ	4861.325	50.2 ± 0.3	7.6 ± 0.05
He I	5015.678	9.2 ± 0.2	0.6 ± 0.03
He I	5875.621	7.1 ± 0.2	0.9 ± 0.08
[O I]	6300.304	12.4 ± 0.6	12.7 ± 0.09
[O I]	6363.776	3.7 ± 0.6	4.2 ± 0.09
Hα	6562.800	364 ± 0.6	152 ± 0.09
He I	6678.151	3.7 ± 0.6	…
[S II]	6730.82	4.1 ± 0.6	6.1 ± 0.09
O I	7773.055	2.6 ± 0.9	…
O I	8446.360	19.4 ± 1.2	6.0 ± 2.0
Ca II	8498.020	217.3 ± 1.2	44.1 ± 1.0
Ca II	8542.090	207.2 ± 1.2	46.3 ± 1.0
Ca II	8662.140	181.9 ± 1.2	38.1 ± 1.0
Pa9	9229.015	15.2 ± 1.8	…

Table 9
UZ Tau E: Observed Lines

2014/12/22			2016/01/25		
Line	λ_{air} (Å)	$F \pm \Delta F$ (10^{-14} erg s^{-1} cm^{-2})	Line	λ_{vac} (Å)	$F \pm \Delta F$ (10^{-14} erg s^{-1} cm^{-2})
H15	3711.977	1.7 ± 0.6	Paδ	10,052.128	59.3 ± 1.6
H14	3721.938	2.5 ± 0.6	He I	10,833.2	68.8 ± 1.0
H13	3734.368	2.5 ± 0.6	Paγ	10,941.090	92.0 ± 0.9
H12	3750.151	3.2 ± 0.6	Paβ	12,821.59	131 ± 0.5
H11	3770.630	3.7 ± 0.6	Br12	16,411.674	16.0 ± 2.3
H10	3797.898	5.0 ± 0.6	Br11	16,811.111	29.7 ± 4.3
H9	3835.384	6.9 ± 0.9	Br10	17,366.850	17.4 ± 2.1
H8	3889.049	8.8 ± 0.7	CO 2-0	22,930	14.5 ± 2.7
Ca II K	3933.660	20.8 ± 0.7	CO 3-1	23,230	18.5 ± 2.7
Ca II H/H7	3968.470	23.1 ± 0.7	⋯	⋯	⋯
He I	4026.191	1.4 ± 0.7	⋯	⋯	⋯
Hδ	4101.702	14.8 ± 0.3	⋯	⋯	⋯
Hγ	4340.464	20.0 ± 0.5	⋯	⋯	⋯
He I	4471.480	3.1 ± 0.5	⋯	⋯	⋯
Hβ	4861.325	42.7 ± 0.3	⋯	⋯	⋯
He I	4921.931	4.9 ± 0.4	⋯	⋯	⋯
He I	5015.678	4.3 ± 0.4	⋯	⋯	⋯
He I	5875.621	7.9 ± 0.4	⋯	⋯	⋯
[O I]	6300.304	14.0 ± 0.4	⋯	⋯	⋯
[O I]	6363.776	3.3 ± 0.4	⋯	⋯	⋯
Hα	6562.800	357 ± 0.4	⋯	⋯	⋯
He I	6678.151	3.6 ± 0.4	⋯	⋯	⋯
[S II]	6730.82	2.1 ± 0.4	⋯	⋯	⋯
He I	7065.190	3.6 ± 0.9	⋯	⋯	⋯
O I	8446.360	22.4 ± 0.9	⋯	⋯	⋯
Ca II	8498.020	92.4 ± 1.0	⋯	⋯	⋯
Ca II	8542.090	81.2 ± 1.0	⋯	⋯	⋯
Ca II	8662.140	78.8 ± 1.0	⋯	⋯	⋯
Pa9	9229.015	17.9 ± 1.3	⋯	⋯	⋯

Table 10
VY Tau: Observed Lines

2014/12/21			2016/03/04		
Line	λ_{air} (Å)	$F \pm \Delta F$ (10^{-14} erg s^{-1} cm^{-2})	Line	λ_{vac} (Å)	$F \pm \Delta F$ (10^{-14} erg s^{-1} cm^{-2})
H10	3797.898	0.16 ± 0.04	He I	10,833.2	0.5 ± 0.1
H9	3835.384	0.19 ± 0.08	CO 2-0	22,930	-9.2 ± 0.7
H8	3889.049	0.33 ± 0.12	CO 3-1	23,230	-3.9 ± 0.7
Ca II K	3933.660	1.94 ± 0.12	⋯	⋯	⋯
Ca II H/H7	3968.470	2.55 ± 0.12	⋯	⋯	⋯
Hδ	4101.702	0.47 ± 0.06	⋯	⋯	⋯
Hγ	4340.464	0.97 ± 0.08	⋯	⋯	⋯
Hβ	4861.325	2.83 ± 0.13	⋯	⋯	⋯
Hα	6562.800	11.3 ± 0.28	⋯	⋯	⋯
Pa9	9229.015	2.37 ± 0.68	⋯	⋯	⋯

Table 11
NY Ori: Observed Lines

		2014/12/21	2016/01/31
Line	λ_{air} (Å)	$F \pm \Delta F$ (10^{-14} erg s^{-1} cm^{-2})	
H15	3711.977	-1.7 ± 0.4	-0.09 ± 0.02
H14	3721.938	-2.2 ± 0.4	-0.15 ± 0.02
H13	3734.368	-2.4 ± 0.6	-0.23 ± 0.02
H12	3750.151	-3.4 ± 0.4	-0.22 ± 0.02
H11	3770.630	-3.0 ± 0.4	-0.23 ± 0.02
H10	3797.898	$1.7(-3.6) \pm 0.4$	-0.44 ± 0.02
H9	3835.384	-5.1 ± 0.4	-0.76 ± 0.02
H8	3889.049	$2.6(-4.1) \pm 0.4$	$0.1(-0.4) \pm 0.02$
Ca II K	3933.660	14.7 ± 0.1	0.6 ± 0.02
Ca II H/H7	3968.470	$11.0(-3.4) \pm 0.1$	$0.4(-0.1) \pm 0.02$
He I	4026.191	1.4 ± 0.1	0.07 ± 0.03
Hδ	4101.702	$3.7(-5.4) \pm 0.3$	$0.3(-0.6) \pm 0.03$
Hγ	4340.464	$4.9(-5.1) \pm 0.3$	$0.4(-0.5) \pm 0.03$
He I	4471.480	1.7 ± 0.3	⋯
Hβ	4861.325	$9.1(-3.6) \pm 0.3$	$0.9(-0.2) \pm 0.03$
He I	4921.931	$2.0(-1.5) \pm 0.1$	⋯
He I	5015.678	$2.0(-2.4) \pm 0.1$	⋯
He I	5875.621	6.5 ± 0.4	0.4 ± 0.04
[O I]	6300.304	0.9 ± 0.3	0.3 ± 0.04
Hα	6562.800	188 ± 0.4	28.7 ± 0.04
He I	6678.151	2.8 ± 0.3	0.3 ± 0.04
O I	8446.360	$4.7(-2.3) \pm 0.2$	$(-0.8) \pm 0.1$
Pa17	8467.253	⋯	$(-0.4) \pm 0.1$
Ca II	8498.020	52.7 ± 0.2	2.4 ± 0.1
Pa16	8502.483	⋯	$(-0.3) \pm 0.1$
Ca II	8542.090	42.4 ± 0.2	1.2 ± 0.1
Pa15	8545.383	⋯	$(-0.5) \pm 0.1$
Pa14	8598.392	2.3 ± 0.3	$(-0.8) \pm 0.1$
Ca II	8662.140	39.0 ± 0.2	1.0 ± 0.1
Pa13	8665.018	⋯	-0.8 ± 0.1
Pa12	8750.472	3.7 ± 0.2	-1.1 ± 0.2
Pa11	8862.783	4.2 ± 0.2	-1.3 ± 0.2
Pa10	9014.910	6.1 ± 0.3	-1.6 ± 0.2
Pa9	9229.015	10.2 ± 0.3	-2.0 ± 0.4

Table 12
V1143 Ori: Observed Lines

	2014/12/21	
Line	λ_{air} (Å)	$F \pm \Delta F$ (10^{-14} erg s^{-1} cm^{-2})
H14	3721.938	0.04 ± 0.01
H13	3734.368	0.05 ± 0.01
H12	3750.151	0.055 ± 0.005
H11	3770.630	0.067 ± 0.005
H10	3797.898	0.111 ± 0.006
H9	3835.384	0.161 ± 0.006
H8	3889.049	0.209 ± 0.006
Ca II K	3933.660	0.371 ± 0.005
Ca II H/H7	3968.470	0.540 ± 0.005
Hδ	4101.702	0.322 ± 0.006
Hγ	4340.464	0.370 ± 0.006
He I	4471.480	0.043 ± 0.006
Hβ	4861.325	0.486 ± 0.005
He I	4921.931	0.058 ± 0.006
He I	5015.678	0.056 ± 0.007
He I	5875.621	0.11 ± 0.01
Hα	6562.800	1.55 ± 0.01

Table 13
DR Tau: Observed Lines

		2014/10/31	2018/03/19		2018/03/23	
Line	λ_{air} (Å)	F $\pm$ ΔF (10^{-14} erg s^{-1} cm^{-2})		Line	λ_{vac} (Å)	$F \pm \Delta F$ (10^{-14} erg s^{-1} cm^{-2})
H18	3691.554	⋯	1.04 ± 0.06	Paδ	10,052.128	70.1 ± 1.8
H17	3697.151	⋯	1.35 ± 0.06	[S II]	10,339.24	4.3 ± 1.8
H16	3703.852	⋯	2.57 ± 0.08	He I	10,833.2	$(-35.7)12.1 \pm 0.1$
H15	3711.977	3.0 ± 0.2	2.90 ± 0.06	Paγ	10,941.090	106.0 ± 1.8
H14	3721.938	4.3 ± 0.3	4.1 ± 0.1	Paβ	12,821.59	173.1 ± 1.8
H13	3734.368	3.5 ± 0.4	4.7 ± 0.1	Br14	15,884.880	10.5 ± 1.6
H12	3750.152	4.4 ± 0.5	4.8 ± 0.1	Br13	16,113.714	15.4 ± 1.6
H11	3770.630	⋯	4.4 ± 0.2	Br12	16,411.674	22.1 ± 1.6
H10	3797.897	⋯	4.9 ± 0.2	Br11	16,811.111	31.5 ± 1.6
H9	3835.384	⋯	5.7 ± 0.1	Br10	17,366.850	36.3 ± 1.6
Ca II K	3933.660	53.5 ± 0.3	18.1 ± 0.1	Brγ	21661.20	31.4 ± 1.8
Ca II H/H7	3968.470	25.3 ± 0.3	$14.0(-0.14) \pm 0.1$	⋯	⋯	⋯
He I	4026.191	2.5 ± 0.4	1.6 ± 0.1	⋯	⋯	⋯
Hδ	4101.702	$(-2.5)3.1 \pm 0.3$	$(-1.4)5.1 \pm 0.1$	⋯	⋯	⋯
Hγ	4340.464	$(-1.6)6.0 \pm 0.3$	$(-1.7)5.0 \pm 0.1$	⋯	⋯	⋯
He I	4471.480	7.5 ± 0.7	4.1 ± 0.1	⋯	⋯	⋯
He II	4685.804	1.9 ± 0.7	1.5 ± 0.1	⋯	⋯	⋯
He I	4713.146	⋯	0.6 ± 0.1	⋯	⋯	⋯
Hβ	4861.325	$(-1.5)30.8 \pm 0.1$	$(-2.2)16.5 \pm 0.1$	⋯	⋯	⋯
He I	4921.931	15.4 ± 0.3	$4.5(-0.4) \pm 0.1$	⋯	⋯	⋯
He I	5015.678	17.0 ± 0.3	$5.5(-0.5) \pm 0.1$	⋯	⋯	⋯
He I	5875.621	15.3 ± 0.3	11.4 ± 0.1	⋯	⋯	⋯
[O I]	6300.304	1.8 ± 0.4	2.4 ± 0.1	⋯	⋯	⋯
Hα	6562.800	407.5 ± 0.5	260.5 ± 0.3	⋯	⋯	⋯
He I	6678.151	7.2 ± 0.4	5.7 ± 0.3	⋯	⋯	⋯
He I	7065.190	6.8 ± 0.4	4.1 ± 0.3	⋯	⋯	⋯
O I	7773.055	12.3 ± 0.4	$2.9(-3.7) \pm 0.4$	⋯	⋯	⋯
Pa25	8323.424	⋯	0.8 ± 0.2	⋯	⋯	⋯
Pa24	8333.782	4.3 ± 0.4	1.2 ± 0.2	⋯	⋯	⋯
Pa23	8345.552	5.0 ± 0.4	1.4 ± 0.2	⋯	⋯	⋯
Pa22	8359.003	5.7 ± 0.5	2.0 ± 0.2	⋯	⋯	⋯
Pa21	8374.475	8.4 ± 0.6	2.2 ± 0.2	⋯	⋯	⋯
Pa20	8392.396	10.7 ± 0.6	2.8 ± 0.2	⋯	⋯	⋯
Pa19	8413.317	10.7 ± 0.5	4.1 ± 0.2	⋯	⋯	⋯
Pa18	8437.955	15.3 ± 0.6	5.3 ± 0.2	⋯	⋯	⋯
O I	8446.360	44.3 ± 0.4	17.9 ± 0.6	⋯	⋯	⋯
Pa17	8467.253	14.3 ± 0.5	5.7 ± 0.6	⋯	⋯	⋯
Ca II	8498.020	237.0 ± 0.4	74.7 ± 0.3	⋯	⋯	⋯
Ca II	8542.090	253.5 ± 0.4	81.8 ± 0.3	⋯	⋯	⋯
Pa14	8598.392	23.8 ± 0.5	13.0 ± 0.3	⋯	⋯	⋯
Ca II	8662.140	214.8 ± 0.4	70.8 ± 0.5	⋯	⋯	⋯
Pa12	8750.472	31.3 ± 0.5	14.9 ± 0.8	⋯	⋯	⋯
Pa11	8862.783	34.4 ± 0.5	19.1 ± 0.8	⋯	⋯	⋯
Pa10	9014.910	39.4 ± 0.5	20.6 ± 0.8	⋯	⋯	⋯
Pa9	9229.015	53.0 ± 0.5	26.5 ± 0.8	⋯	⋯	⋯
Pa8	9545.971	63.1 ± 2	34.7 ± 1.3	⋯	⋯	⋯

Table 14
ASASSN-13db: Observed Lines

		2014/12/21	2015/10/01	2017/02/21			2015/02/10
Line	λ_{air} (Å)	$F\pm\Delta F$ (10^{-14} erg s^{-1} cm^{-2})			Line	λ_{vac} (Å)	$F\pm\Delta F$ (10^{-14} erg s^{-1} cm^{-2})
H9	3835.384	⋯	⋯	0.10 ± 0.02	He I	10,833.2	$(-13.3)\pm0.1$
Ca II K	3933.660	$(-1.9)1.2\pm0.2$	$(-1.3)6.2\pm0.3$	$(-0.01)0.21\pm0.01$	Paβ	12821.59	5.7 ± 1.5
Ca II H/H7	3968.470	$(-1.0)0.9\pm0.2$	$(-1.5)3.6\pm0.3$	$(-0.01)0.32\pm0.01$	⋯	⋯	⋯
Hδ	4101.702	⋯	⋯	0.25 ± 0.01	⋯	⋯	⋯
Hγ	4340.464	⋯	⋯	0.31 ± 0.01	⋯	⋯	⋯
Hβ	4861.325	-2.6 ± 0.2	-3.0 ± 0.3	0.47 ± 0.01	⋯	⋯	⋯
He I	4921.931	⋯	⋯	0.08 ± 0.01	⋯	⋯	⋯
He I	5015.678	⋯	⋯	0.07 ± 0.01	⋯	⋯	⋯
He I	5875.621	⋯	⋯	0.08 ± 0.01	⋯	⋯	⋯
[O I]	6300.304	⋯	⋯	0.09 ± 0.01	⋯	⋯	⋯
[O I]	6363.776	⋯	⋯	0.04 ± 0.01	⋯	⋯	⋯
Hα	6562.800	$(-1.4)11.5\pm1.0$	$(-1.4)27.3\pm0.4$	1.21 ± 0.01	⋯	⋯	⋯
He I	6678.151	⋯	⋯	0.06 ± 0.01	⋯	⋯	⋯
[S II]	6716.44	⋯	⋯	0.08 ± 0.01	⋯	⋯	⋯
[S II]	6730.82	⋯	⋯	0.18 ± 0.01	⋯	⋯	⋯
Ca II	8498.020	13.1 ± 0.3	12.8 ± 0.4	0.23 ± 0.01	⋯	⋯	⋯
Ca II	8542.090	13.5 ± 0.3	13.2 ± 0.4	0.24 ± 0.01	⋯	⋯	⋯
Ca II	8662.140	10.2 ± 0.3	9.8 ± 0.4	0.19 ± 0.01	⋯	⋯	⋯

Table 15
V1647 Ori: Observed Lines

	2016/01/26	
Line	$\lambda_{air/vac}$ (Å)	$F\pm\Delta F$ (10^{-14} erg s^{-1} cm^{-2})
[O I]	6300.304	0.22 ± 0.06
Hα	6562.800	$(-0.04)0.60\pm0.02$
O I	7773.055	0.03 ± 0.04
O I	8446.360	0.18 ± 0.04
Ca II	8498.020	1.09 ± 0.04
Ca II	8542.090	1.20 ± 0.04
Ca II	8662.140	1.09 ± 0.04
Paδ	10,052.128	2.8 ± 0.3
He I	10,833.2	$(-29.8)\pm1.0$
Paγ	10,941.090	10.3 ± 1.0
Paβ	12,821.59	73.2 ± 2.0

Table 16
iPTF15afq: Observed Lines

		2016/01/27	2017/02/15			2018/01/28	2019/12/02
Line	λ_{air} (Å)	$F \pm \Delta F$ (10^{-14} erg s^{-1} cm^{-2})		Line	λ_{vac} (Å)	$F \pm \Delta F$ (10^{-14} erg s^{-1} cm^{-2})	
[O I]	6300.304	0.35 ± 0.01	0.21 ± 0.01	Paδ	10,052.128	0.46 ± 0.02	-0.6 ± 0.1
[O I]	6363.776	0.11 ± 0.01	0.08 ± 0.01	[S II]	10,320.49	0.10 ± 0.02	⋯
Hα	6562.800	1.46 ± 0.01	1.14 ± 0.01	[S II]	10,336.41	0.16 ± 0.02	⋯
[NII]	6583.46	0.03 ± 0.01	⋯	He I	10,833.2	0.62 ± 0.02	-2.2 ± 0.1
[S II]	6716.44	0.04 ± 0.01	0.03 ± 0.01	Paγ	10,941.090	0.67 ± 0.02	-1.6 ± 0.2
[S II]	6730.82	0.08 ± 0.01	0.06 ± 0.01	[Fe II]	12,570.2068	0.26 ± 0.02	⋯
[Fe II]	7155.1742	0.14 ± 0.01	0.09 ± 0.01	Paβ	12,821.59	1.61 ± 0.02	-1.9 ± 0.2
[Fe II]	7167.9228	0.04 ± 0.01	⋯	Br8	19,450.871	0.6 ± 0.1	⋯
[Fe II]	7288.9899	0.05 ± 0.01	⋯	H2 1-0S(1)	21,218.	0.12 ± 0.02	⋯
[Ca II]	7323.89	0.10 ± 0.01	⋯	Brγ	21,661.20	0.54 ± 0.04	⋯
[NiII]	7377.83	0.08 ± 0.01	⋯	CO 2-0	22,930	2.9 ± 0.2	⋯
[Fe II]	7388.1673	0.05 ± 0.01	⋯	CO 3-1	23,230	3.8 ± 0.2	$(-4.0)3.6 \pm 0.5$
[NiII]	7411.61	0.04 ± 0.01	⋯	⋯	⋯	⋯	⋯
[Fe II]	7452.5611	0.06 ± 0.01	⋯	⋯	⋯	⋯	⋯
[Fe II]	8387.181	0.09 ± 0.01	⋯	⋯	⋯	⋯	⋯
[Fe II]	8446.360	5.13 ± 0.01	0.08 ± 0.01	⋯	⋯	⋯	⋯
Pa17	8467.253	0.04 ± 0.01	⋯	⋯	⋯	⋯	⋯
Ca II	8498.020	8.15 ± 0.01	1.01 ± 0.01	⋯	⋯	⋯	⋯
Ca II	8542.090	9.84 ± 0.01	1.07 ± 0.01	⋯	⋯	⋯	⋯
Pa14	8598.392	0.03 ± 0.01	⋯	⋯	⋯	⋯	⋯
Ca II	8662.140	0.89 ± 0.01	⋯	⋯	⋯	⋯	⋯
Pa12	8750.472	0.04 ± 0.01	⋯	⋯	⋯	⋯	⋯
Pa11	8862.783	0.06 ± 0.01	⋯	⋯	⋯	⋯	⋯
Pa10	9014.910	0.09 ± 0.01	⋯	⋯	⋯	⋯	⋯
Pa9	9229.015	0.18 ± 0.02	0.12 ± 0.04	⋯	⋯	⋯	⋯
Pa8	9545.971	0.14 ± 0.02	⋯	⋯	⋯	⋯	⋯

Table 17
PV Cep: Observed Lines

		2015/06/24			2016/12/08
Line	λ_{air} (Å)	$F \pm \Delta F$ (10^{-14} erg s^{-1} cm^{-2})	Line	λ_{vac} (Å)	$F \pm \Delta F$ (10^{-14} erg s^{-1} cm^{-2})
H15	3711.977	-0.05 ± 0.02	Pa8	9548.590	32 ± 2
H14	3721.938	-0.13 ± 0.02	Paδ	10,052.128	48 ± 2
H13	3734.368	-0.10 ± 0.02	[S II]	10,320.49	36 ± 3
H12	3750.151	-0.10 ± 0.02	[NI]	10,400.59	20 ± 3
H11	3770.630	-0.10 ± 0.02	He I	10,833.2	-43 ± 1
H10	3797.898	-0.15 ± 0.02	Paγ	10,941.090	61 ± 3
H9	3835.384	-0.22 ± 0.02	Paβ	12,821.59	210 ± 2
H8	3889.049	-0.38 ± 0.02	Br14	15,884.880	34 ± 5
Ca II K	3933.660	(-0.04) 0.73 ± 0.02	Br13	16,113.714	50 ± 5
Ca II H/H7	3968.470	-0.28 ± 0.02	Br12	16,411.674	60 ± 5
Hδ	4101.702	-0.23 ± 0.02	Br11	16,811.111	65 ± 5
Hγ	4340.464	-0.39 ± 0.02	Br10	17,366.850	72 ± 10
Hβ	4861.325	(-0.39) 1.58 ± 0.02	Brγ	21,661.20	49 ± 8
He I	4921.931	0.61 ± 0.04	C0 2-0	22,930	161 ± 20
He I	5015.678	0.47 ± 0.04	⋯	⋯	⋯
[O I]	6300.304	4.68 ± 0.07	⋯	⋯	⋯
[O I]	6363.776	1.61 ± 0.07	⋯	⋯	⋯
Hα	6562.800	52.8 ± 0.04	⋯	⋯	⋯
He I	6678.151	0.65 ± 0.04	⋯	⋯	⋯
O I	7773.055	2.11 ± 0.09	⋯	⋯	⋯
Pa19	8413.317	2.00 ± 0.09	⋯	⋯	⋯
Pa18	8437.955	2.51 ± 0.09	⋯	⋯	⋯
O I	8446.360	13.9 ± 0.09	⋯	⋯	⋯
Pa17	8467.253	3.97 ± 0.09	⋯	⋯	⋯
Ca II	8498.020	79.6 ± 0.09	⋯	⋯	⋯
Ca II	8542.090	69.4 ± 0.09	⋯	⋯	⋯
Pa14	8598.392	4.41 ± 0.09	⋯	⋯	⋯
Ca II	8662.140	61.9 ± 0.09	⋯	⋯	⋯
Pa12	8750.472	5.81 ± 0.09	⋯	⋯	⋯
Pa11	8862.783	6.34 ± 0.09	⋯	⋯	⋯
Pa10	9014.910	7.22 ± 0.13	⋯	⋯	⋯
Pa9	9229.015	8.16 ± 0.13	⋯	⋯	⋯

Table 18
V350 Cep: Observed Lines

		2015/11/08	2018/09/29			2019/07/04	2019/10/02	2019/10/17
Line	λ_{vac} (Å)	$F \pm \Delta F$ (10^{-14} erg s^{-1} cm^{-2})		Line	λ_{air} (Å)	$F \pm \Delta F$ (10^{-14} erg s^{-1} cm^{-2})		
Paδ	10052.128	2.8 ± 0.2	1.1 ± 0.1	Ca II K	3933.660	1.48 ± 0.08	2.17 ± 0.03	2.24 ± 0.02
[S II]	10320.49	1.2 ± 0.2	⋯	Ca II H/H7	3968.470	0.85 ± 0.07	0.67 ± 0.03	1.03 ± 0.02
He I	10833.2	-2.2 ± 0.1	-1.2 ± 0.1	Hδ	4101.702	0.27 ± 0.07	0.48 ± 0.08	0.48 ± 0.03
Paγ	10941.090	2.9 ± 0.1	1.5 ± 0.1	Hγ	4340.464	0.32 ± 0.05	0.65 ± 0.08	0.58 ± 0.03
Paβ	12821.59	4.1 ± 0.1	1.6 ± 0.1	Hβ	4861.325	0.78 ± 0.04	$(-0.09)1.50 \pm 0.02$	1.45 ± 0.03
Br12	16411.674	1.4 ± 0.2	⋯	He I	4921.931	0.39 ± 0.05	0.61 ± 0.02	0.63 ± 0.03
Br11	16811.111	1.9 ± 0.5	⋯	He I	5015.678	0.35 ± 0.03	0.54 ± 0.04	0.55 ± 0.03
Br10	17366.850	1.0 ± 0.2	⋯	[O I]	6300.304	0.88 ± 0.04	0.96 ± 0.01	1.24 ± 0.04
H2 1-0S(1)	21218.	0.38 ± 0.02	⋯	[O I]	6363.776	0.30 ± 0.04	0.37 ± 0.01	0.36 ± 0.04
Brγ	21661.20	0.97 ± 0.07	⋯	Hα	6562.800	9.76 ± 0.04	16.1 ± 0.01	15.0 ± 0.04
⋯	⋯	⋯	⋯	He I	6678.151	0.14 ± 0.04	0.19 ± 0.01	0.17 ± 0.04
⋯	⋯	⋯	⋯	O I	7773.055	0.46 ± 0.09	0.43 ± 0.01	0.49 ± 0.04
⋯	⋯	⋯	⋯	Pa19	8413.317	0.07 ± 0.02	0.06 ± 0.02	⋯
⋯	⋯	⋯	⋯	Pa18	8437.955	0.10 ± 0.02	⋯	⋯
⋯	⋯	⋯	⋯	O I	8446.360	0.59 ± 0.02	0.92 ± 0.06	0.77 ± 0.05
⋯	⋯	⋯	⋯	Pa17	8467.253	0.33 ± 0.02	0.32 ± 0.06	0.35 ± 0.05
⋯	⋯	⋯	⋯	Ca II	8498.020	7.04 ± 0.02	6.95 ± 0.06	7.93 ± 0.05
⋯	⋯	⋯	⋯	Ca II	8542.090	8.17 ± 0.02	8.14 ± 0.06	9.27 ± 0.05
⋯	⋯	⋯	⋯	Pa14	8598.392	0.35 ± 0.04	0.41 ± 0.06	0.40 ± 0.05
⋯	⋯	⋯	⋯	Ca II	8662.140	7.48 ± 0.04	7.30 ± 0.06	8.16 ± 0.05
⋯	⋯	⋯	⋯	Pa12	8750.472	0.46 ± 0.04	0.56 ± 0.06	0.46 ± 0.05
⋯	⋯	⋯	⋯	Pa11	8862.783	0.47 ± 0.04	0.50 ± 0.06	0.55 ± 0.05
⋯	⋯	⋯	⋯	Pa10	9014.910	0.6 ± 0.1	0.63 ± 0.06	1.04 ± 0.06
⋯	⋯	⋯	⋯	Pa9	9229.015	1.0 ± 0.1	0.97 ± 0.07	1.4 ± 0.2

Appendix B
Veiling Determination

In this section, we briefly discuss the strategy we adopted to estimate the veiling (r) in our sample. For a given source, we have first selected a number of BTSettl templates with temperature within 500 K of the $T_{\rm eff}$ value given in the literature (Table 3) and log$g$ between 3.5 and 4.5. A veiling (increasing in steps of 0.1) is then added to each template to find the value that best matches the spectral features observed in our sample of stars.

For M-type stars, which are the majority of our sources, we have fitted the portion of the continuum in the range 700–715 nm, where prominent TiO absorption bands are located (Figure 12). In all sources but two, our fit consistently provides a $T_{\rm eff}$ in agreement with that of the literature, and determined r with a typical error of 0.3, corresponding to a variation of $T_{\rm eff}$ less than 100 K. The two exceptions are UZ Tau E and V1143 Ori ($T_{\rm eff}$ of literature 3410 K and 3500 K, respectively). In the case of UZ Tau E, we have accurate determinations of $T_{\rm eff} = 3600$ K and $r = 0.7$ from high-resolution observations obtained with the HARPS-N instrument at the *Telescopio Nazionale Galileo* (Gangi et al., in preparation). Having assumed the veiling value, we have fitted $T_{\rm eff}$ in the MODS spectrum, which is in perfect agreement with that derived from the HARPS-N spectrum (Figure 13). In the case of V1143 Ori, we fit $T_{\rm eff} = 3200$ K and $r = 0$. Since for $r > 0$ $T_{\rm eff}$ is even lower, the literature value cannot be reproduced.

For the few sources that do not present the TiO bands because of their SpT (in particular NY Ori, DR Tau, and PV Cep), we applied an indirect method to evaluate the veiling at 710 nm. We first reddened the BTSettl template by assuming the A_V derived from the "line method" (Section 6.1.1). By dividing the observed spectrum with the reddened template, we have derived the shape of the excess continuum flux. The ratio at 710 nm was then assumed as the veiling value, reported in Table 6.

We also looked for TiO spectral variations in the three sources of this subsample that were observed more than once (XZ Tau, V350 Cep, and ASASSN13-db, see Figure 14). We have found that XZ Tau shows an increase in the depth of the TiO bands between 2014 and 2018 which corresponds to a decrease in r from 0.8 to 0.0. TiO bands do not appear in the spectra of ASASSN13-db during the burst phases of 2014 and 2015 while they are present during the out-of-burst phase of 2017 with a corresponding veiling of 0.4. The absence of TiO bands in 2014 and 2015 indicates that during the outburst the veiling increased to values larger than 3. Finally, the veiling measured in V350 Cep does not show variations that exceed the quoted uncertainty of 0.3.

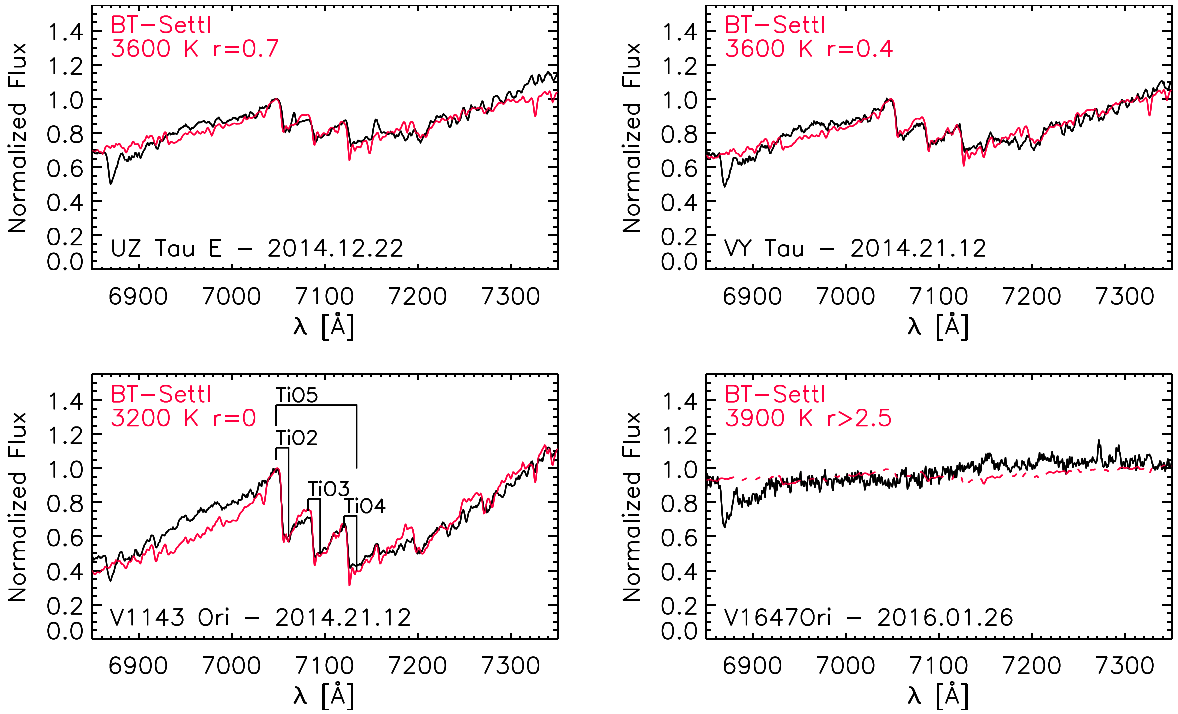

Figure 12. Examples of BTSettl models best matching the TiO bands. Spectra are normalized to the peak of the band. For each panel, object name, date of observation, temperature of the BTSettl model, and veiling are reported. In the third panel, TiO bands are indicated.

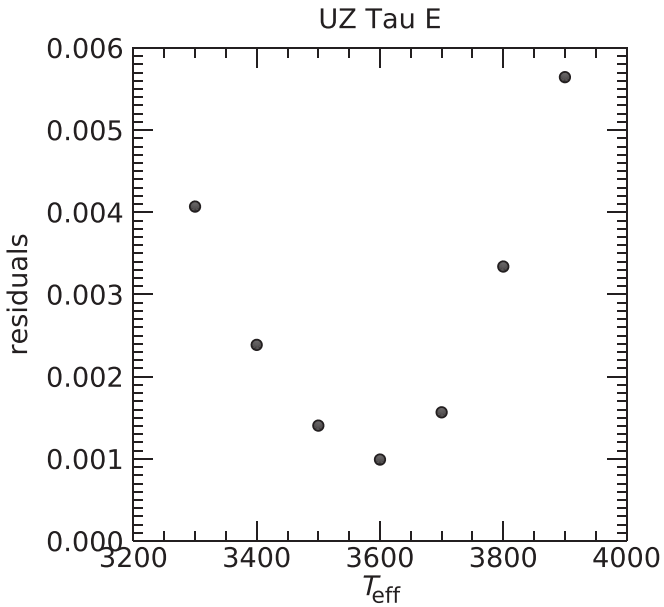

Figure 13. Residuals on $T_{\rm eff}$ fitting in UZ Tau E, assuming $r = 0.7$. The BTSettl model that best matches the MODS spectrum corresponds to $T_{\rm eff} = 3600$ K, the same as that found with high-spectral resolution observations.

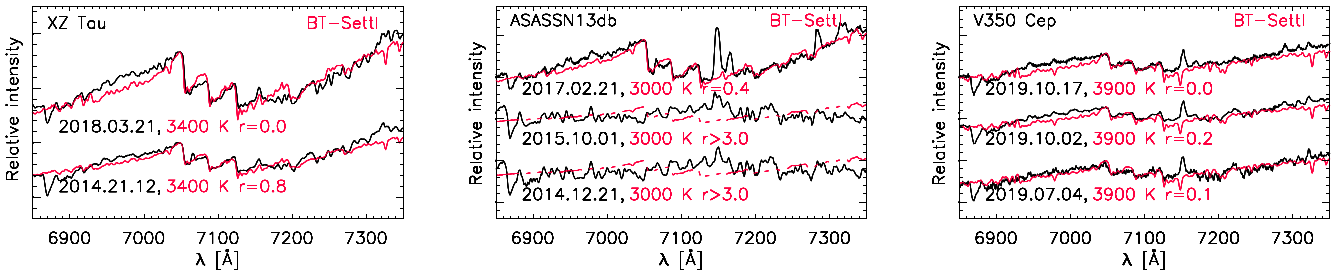

Figure 14. TiO bands strength variability. Spectra are normalized to the peak of the band and vertically shifted for a better visualization. Date of observation, temperature of the best matching BTSettl model, and veiling are also labeled.

ORCID iDs

T. Giannini https://orcid.org/0000-0002-7035-8513
M. Gangi https://orcid.org/0000-0002-8364-7795
D. Lorenzetti https://orcid.org/0000-0001-6415-4162
S. Antoniucci https://orcid.org/0000-0002-0666-3847
B. Nisini https://orcid.org/0000-0002-9190-0113
V. Testa https://orcid.org/0000-0003-1033-1340

References

Akeson, R. L., Jensen, E. L. N., Carpenter, J., et al. 2019, ApJ, 872, 158
Alcalá, J. M., Gangi, M. E., Biazzo, K., et al. 2021, A&A, 652, A72
Alcalá, J. M., Manara, C. F., Natta, A., et al. 2017, A&A, 600, A20
Alcalá, J. M., Natta, A., Manara, C. F., et al. 2014, A&A, 561, A2
Andrews, S. M., Rothberg, B., & Simon, T. 2004, ApJL, 610, L45
Andreasyan, H. R., Magakian, T. Y., Movsessian, T. A., & Moiseev, A. V. 2021, Ap, 64, 187
Antoniucci, S., Arkharov, A. A., Di Paola, A., et al. 2013, in Protostars and Planets VI, Poster #2B055 (Tucson, AZ: Univ. Arizona Press)
Antoniucci, S., García López, R., Nisini, B., et al. 2014, A&A, 572, A62
Antoniucci, S., Nisini, B., Biazzo, K., et al. 2017a, A&A, 606, A48
Antoniucci, S., Nisini, B., Giannini, T., et al. 2017b, A&A, 599, A105
Arce, H. G., Borkin, M. A., Goodman, A. A., Pineda, J. E., & Halle, M. W. 2010, ApJ, 715, 1170
Armitage, P. J. 2016, ApJL, 833, L15
Aspin, C. 2011, AJ, 142, 135
Aspin, C., Barbieri, C., Boschi, F., et al. 2006, AJ, 132, 1298
Aspin, C., Beck, T. L., & Reipurth, B. 2008, AJ, 135, 423
Aspin, C., Greene, T. P., & Reipurth, B. 2009, AJ, 137, 2968
Aspin, C., & Reipurth, B. 2009, AJ, 138, 1137
Audard, M., Ábrahám, P., Dunham, M. M., et al. 2014, in Protostars and Planets VI, ed. H. Beuther et al. (Tucson, AZ: Univ. Arizona Press), 387
Audard, M., Stringfellow, G. S., Güdel, M., et al. 2010, A&A, 511, A63
Banzatti, A., Meyer, M. R., Manara, C. F., Pontoppidan, K. M., & Testi, L. 2014, ApJ, 780, 26
Banzatti, A., Pascucci, I., Edwards, S., et al. 2019, ApJ, 870, 76
Biscaya, A. M., Rieke, G. H., Narayanan, G., Luhman, K. L., & Young, E. T. 1997 ApJ, 491, 359
Bonnell, I., & Bastien, P. 1992, ApJL, 401, L31
Briceño, C., Vivas, A. K., Hernández, J., et al. 2004, ApJL, 606, L123
Cabrit, S., Edwards, S., Strom, S. E., & Strom, K. M. 1990, ApJ, 354, 687
Caratti o Garatti, A., Garcia Lopez, R., Weigelt, G., et al. 2013, A&A, 554, A66
Cardelli, J. A., Clayton, G. C., & Mathis, J. S. 1989, ApJ, 345, 245
Chavarria, K. C. 1979, A&A, 79, L18
Cieza, L. A., Ruíz-Rodríguez, D., Perez, S., et al. 2018, MNRAS, 474, 4347
Coffey, D., Downes, T. P., & Ray, T. P. 2004, A&A, 419, 593
Cohen, M., Kuhi, L. V., Spinrad, H., & Harlan, E. A. 1981, ApJ, 245, 920
Connelley, M. S., & Reipurth, B. 2018, ApJ, 861, 145
Contreras Peña, C., Lucas, P. W., Kurtev, R., et al. 2017, MNRAS, 465, 3039
Contreras Peña, C., Naylor, T., & Morrell, S. 2019, MNRAS, 486, 4590
Costigan, G., Vink, J. S., Scholz, A., Ray, T., & Testi, L. 2014, MNRAS, 440, 3444
Csépány, G., van den Ancker, M., Ábrahám, P., et al. 2017, A&A, 603, A74
D'Angelo, C. R., & Spruit, H. C. 2012, MNRAS, 420, 416
Dodin, A. V., Emelyanov, N. V., Zharova, A. V., et al. 2016, AstL, 42, 29
Edwards, S., Kwan, J., Fischer, W., et al. 2013, ApJ, 778, 148
Fiorellino, E., Manara, C. F., Nisini, B., et al. 2021, A&A, 650, A43
Fischer, W., Edwards, S., Hillenbrand, L., & Kwan, J. 2011, ApJ, 730, 73
Fischer, W. J., Padgett, D. L., Stapelfeldt, K. L., & Sewiło, M. 2016, ApJ, 827, 96
Folha, D. F. M., & Emerson, J. P. 2001, A&A, 365, 90
Gaia Collaboration, Klioner, S. A., Mignard, F., et al. 2021, A&A, 649, A9
Gaia Collaboration, Prusti, T., de Bruijne, J. H. J., et al. 2016, A&A, 595, A1
Giannini, T., Antoniucci, S., Lorenzetti, D., et al. 2017, ApJ, 839, 112
Giannini, T., Giunta, A., Lorenzetti, D., et al. 2020, A&A, 637, A83
Giannini, T., Lorenzetti, D., Antoniucci, S., et al. 2016, ApJL, 819, L5
Giannini, T., Munari, U., Antoniucci, S., et al. 2018, A&A, 611, A54
Giannini, T., Nisini, B., Antoniucci, S., et al. 2019, A&A, 631, A44
Gramajo, L. V., Rodón, J. A., & Gómez, M. 2014, AJ, 147, 140
Grankin, K. N., Artemenko, S. A., & Melnikov, S. Y. 2007, IBVS, 5752, 1
Grankin, K. N., Bouvier, J., Herbst, W., & Melnikov, S. Y. 2008, A&A, 479, 827
Gullbring, E., Hartmann, L., Briceño, C., & Calvet, N. 1998, ApJ, 492, 323
Guo, Z., Lucas, P. W., Contreras Peña, C., et al. 2020, MNRAS, 492, 294
Hamidouche, M. 2010, ApJ, 722, 204
Hartigan, P., & Kenyon, S. J. 2003, ApJ, 583, 334
Hartmann, L., & Kenyon, S. J. 1985, ApJ, 299, 462
Hartmann, L., Kenyon, S., & Hartigan, P. 1993, in Protostars and Planets III, ed. E. H. Levy & J. I. Lunine (Tucson, AZ: Univ. Arizona Press), 497
Herbig, G. H. 1989, in ESO Workshop on Low Mass Star Formation and Pre-Main Sequence Objects 33 (Garching: ESO), 233
Herbig, G. H. 1990, ApJ, 360, 639
Herbig, G. H. 2008, AJ, 135, 637
Herbig, G. H., & Bell, K. R. 1988, in Third Catalog of Emission-line Stars of the Orion Population, Lick Observatory Bulletin #1111, ed. G. H. Gerbig & K. R. Bell (Santa Cruz: Lick Observatory), 90, Jun 1988
Herczeg, G. J., & Hillenbrand, L. A. 2014, ApJ, 786, 97
Hillenbrand, L. A. 1997, AJ, 113, 1733
Hillenbrand, L. A. 2019, ATel, 13321, 1
Hillenbrand, L. A., Miller, A. A., Covey, K. R., et al. 2013, AJ, 145, 59
Holoien, T. W.-S., Prieto, J. L., Stanek, K. Z., et al. 2014, ApJL, 785, L35
Jensen, E. L. N., Dhital, S., Stassun, K. G., et al. 2007, AJ, 134, 241
Joncour, I., Duchêne, G., & Moraux, E. 2017, A&A, 599, A14
Jurdana-Šepić, R., Munari, U., Antoniucci, S., et al. 2017, A&A, 602, A99
Jurdana-Šepić, R., Munari, U., Antoniucci, S., Giannini, T., & Lorenzetti, D. 2018, A&A, 614, A9
Kenyon, S. J., Hartmann, L., Hewett, R., et al. 1994, AJ, 107, 2153
Kóspál, Á., Ábrahám, P., Acosta-Pulido, J. A., et al. 2016, A&A, 596, A52
Kounkel, M., Covey, K., Moe, M., et al. 2019, AJ, 157, 196
Kuffmeier, M., Frimann, S., Jensen, S. S., & Haugbølle, T. 2018, MNRAS, 475, 2642
Kun, M., Balog, Z., Kenyon, S. J., Mamajek, E. E., & Gutermuth, R. A. 2009, ApJS, 185, 451
Kun, M., Moór, A., Szegedi-Elek, E., & Reipurth, B. 2016, ApJ, 822, 79
Kun, M., Szegedi-Elek, E., Moór, A., et al. 2011, MNRAS, 413, 2689
Kwan, J., & Fischer, W. 2011, MNRAS, 411, 2383
Leinert, C., Zinnecker, H., Weitzel, N., et al. 1993, A&A, 278, 129
Li, H., Li, D., Qian, L., et al. 2015, ApJS, 219, 20
Lodato, G., & Clarke, C. J. 2004, MNRAS, 353, 841
Lorenzetti, D., Antoniucci, S., Giannini, T., et al. 2015, ApJ, 802, 24
Lorenzetti, D., Giannini, T., Larionov, V. M., et al. 2007, ApJ, 665, 1182
Lorenzetti, D., Giannini, T., Larionov, V. M., et al. 2011, ApJ, 732, 69
Lorenzetti, D., Larionov, V. M., Giannini, T., et al. 2009, ApJ, 693, 1056
Luhman, K. L., Allen, P. R., Espaillat, C., Hartmann, L., & Calvet, N. 2010, ApJS, 186, 111
MacFarlane, B., Stamatellos, D., Johnstone, D., et al. 2019a, MNRAS, 487, 4465
MacFarlane, B., Stamatellos, D., Johnstone, D., et al. 2019b, MNRAS, 487, 5106
Magakian, T. Y., & Movsesian, T. A. 2001, Ap, 44, 419
Manara, C. F., Beccari, G., Da Rio, N., et al. 2013, A&A, 558, A114
Manara, C. F., Testi, L., Herczeg, G. J., et al. 2017, A&A, 604, A127
Meng, H. Y. A., Rieke, G. H., Kim, J. S., et al. 2019, ApJ, 878, 7
Meyer, M. R., Calvet, N., & Hillenbrand, L. A. 1997, AJ, 114, 288
Miller, A. A., Hillenbrand, L. A., Bilgi, P., et al. 2015, ATel, 7428, 1
Moody, M. S. L., & Stahler, S. W. 2017, A&A, 600, A133
Morales-Calderón, M., Stauffer, J. R., Hillenbrand, L. A., et al. 2011, ApJ, 733, 50
Moura, T., Alencar, S. H. P., Sousa, A. P., Alecian, E., & Lebreton, Y. 2020, MNRAS, 494, 3512
Muzerolle, J., Hillenbrand, L., Calvet, N., Briceño, C., & Hartmann, L. 2003, ApJ, 592, 266
Nisini, B., Giannini, T., Antoniucci, S., et al. 2016, A&A, 595, A76
Osorio, M., Macías, E., Anglada, G., et al. 2016, ApJL, 825, L10
Petrov, P. P., Gahm, G. F., Stempels, H. C., Walter, F. M., & Artemenko, S. A. 2011, A&A, 535, A6
Pogge, R. W., Atwood, B., Brewer, D. F., et al. 2010, Proc. SPIE, 7735, 77350A
Principe, D. A., Cieza, L., Hales, A., et al. 2018, MNRAS, 473, 879
Rodrigo, C., & Solano, E. 2020, in Contributions to the XIV.0 Scientific Meeting (virtual) of the Spanish Astronomical Society (Barcelona: Spanish Astronomical Society), 182, https://www.sea-astronomia.es/reunion-cientifica-2020
Schipani, P., Campana, S., Claudi, R., et al. 2018, Proc. SPIE, 10702, 107020F
Seifert, W., Appenzeller, I., Baumeister, H., et al. 2003, Proc. SPIE, 4841, 962
Semkov, E. H., Ibryamov, S. I., & Peneva, S. P. 2017, BlgAJ, 27, 75

Shu, F. H., Najita, J., Ruden, S. P., & Lizano, S. 1994, ApJ, 429, 797
Sicilia-Aguilar, A., Kóspál, Á., Setiawan, J., et al. 2012, A&A, 544, A93
Sicilia-Aguilar, A., Oprandi, A., Froebrich, D., et al. 2017, A&A, 607, A127
Sipos, N., Ábrahám, P., Acosta-Pulido, J., et al. 2009, A&A, 507, 881
Sipos, N., & Kóspál, Á. 2014, in IAU Symp. 299, Exploring the Formation and Evolution of Planetary Systems (Cambridge: Cambridge Univ. Press), 121
Sperling, T., Eislöffel, J., Fischer, C., et al. 2020, A&A, 642, A216
Stock, C., Caratti o Garatti, A., McGinnis, P., et al. 2020, A&A, 643, A181
Stone, R. P. S. 1983, IBVS, 2380, 1
The, P. S., de Winter, D., & Perez, M. R. 1994, A&AS, 104, 315
Weingartner, J. C., & Draine, B. T. 2001, ApJ, 548, 296
Yang, H., Herczeg, G. J., Linsky, J. L., et al. 2012, ApJ, 744, 121
Young, K. E., Young, C. H., Lai, S.-P., Dunham, M. M., & Evans, N. J., II 2015, AJ, 150, 40